nature

https://doi.org/10.1038/s41586-019-1782-2

Supplementary information

Molecular tuning of CO2-to-ethylene conversion

In the format provided by the authors and unedited

Fengwang Li, Arnaud Thevenon, Alonso Rosas-Hernández, Ziyun Wang, Yilin Li, Christine M. Gabardo, Adnan Ozden, Cao Thang Dinh, Jun Li, Yuhang Wang, Jonathan P. Edwards, Yi Xu, Christopher McCallum, Lizhi Tao, Zhi-Qin Liang, Mingchuan Luo, Xue Wang, Huihui Li, Colin P. O'Brien, Chih-Shan Tan, Dae-Hyun Nam, Rafael Quintero-Bermudez, Tao-Tao Zhuang, Yuguang C. Li, Zhiji Han, R. David Britt, David Sinton, Theodor Agapie, Jonas C. Peters & Edward H. Sargent

Supplementary Information for

Intermediate stabilization via molecular tuning for CO_2-to-ethylene conversion

Fengwang Li[1]*, Arnaud Thevenon[2]*, Alonso Rosas-Hernández[2]*, Ziyun Wang[1]*, Yilin Li[1]*, Christine M. Gabardo[3], Adnan Ozden[3], Cao Thang Dinh[1], Jun Li[1,3], Yuhang Wang[1], Jonathan P. Edwards[3], Yi Xu[3], Christopher McCallum[3], Lizhi Tao[4], Zhi-Qin Liang[1], Mingchuan Luo[1], Xue Wang[1], Huihui Li[1], Colin P. O'Brien[3], Chih-Shan Tan[1], Dae-Hyun Nam[1], Rafael Quintero-Bermudez[1], Tao-Tao Zhuang[1], Yuguang C. Li[1], Zhiji Han[2], R. David Britt[4], David Sinton[3], Theodor Agapie[2], Jonas C. Peters[2], Edward H. Sargent[1]

[1]*Department of Electrical and Computer Engineering, University of Toronto, 35 St George Street, Toronto, Ontario M5S 1A4, Canada*

[2]*Division of Chemistry and Chemical Engineering, California Institute of Technology, Pasadena, California 91125, USA*

[3]*Department of Mechanical and Industrial Engineering, University of Toronto, 5 King's College Road, Toronto, Ontario, M5S 3G8, Canada*

[4]*Department of Chemistry, University of California, Davis, California 95616, USA*

*These authors contributed equally to this work.

Methods

Molecule synthesis. All solvents and reagents were obtained from commercial sources (Aldrich and Merck) and used as received, unless stated otherwise. D_2O (D 99.5 %), *d*-chloroform (D 99.8%) and d_6-DMSO (D 99.8%) were purchased from Cambridge Isotope Laboratories. The ^1H and ^{13}C NMR spectra were recorded on a Bruker 400 MHz instrument with a prodigy broadband cryoprobe. Shifts were reported relative to the residual solvent peak.

The ^1H and ^{13}C NMR spectra of all the reported salts and their corresponding precursors were in agreement with the reported literature[1-4]. Molecules **7**, **8**, **9**, **10** and **11** are new and were fully characterized by multinuclear NMR spectroscopy. All the salts were recrystallized at least one time from MeOH/Ether (1:5) prior to use for electrochemical experiments.

In a typical procedure for the synthesis of aryl-pyridinium chloride salts[1,2], Zincke salt [1-(2,4-dinitrophenyl)-pyridinium chloride] (2.0 mmol, 1 equiv.), *para*-substituted aniline (4.0 mmol, 2 equiv.), were dissolved in EtOH/H_2O (60/40, 10 mL) and charged into a microwave vial (40 mL) equipped with a magnetic stir bar. The vial was sealed, and the reaction was performed under microwaves at 130 °C for 35 min. After reaction, the mixture was concentrated under vacuum. The red solid was purified by flush column chromatography (silica; MeCN to MeOH). Yield: 0.35 g (62%).

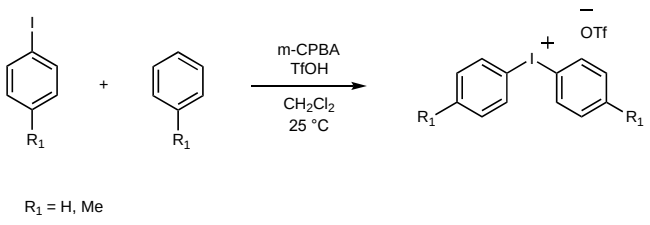

Scheme 1 | Synthesis of aryliodonium triflate salts.

As shown in Scheme 1, in a typical procedure for the synthesis of aryliodonium triflate salts[5] for R_1 = H or Me, the *para*-iodoaryl precursor (10 g, 1 equiv.), the corresponding arene (R = H: benzene; R = Me: toluene, 1.1 equiv.) and *m*-CPBA (70 % active oxidant, 1.1 equiv.) were dissolved in DCM (100 mL) in a round bottom flask equipped with a magnetic stir bar.

TfOH (2.1 equiv.) was added dropwise at 0 °C yielding a yellow solution. A precipitate was formed upon stirring the reaction for 4 h, at 25 °C. The precipitate was filtered off and ether was added to the filtrate. The desired product crashed out as a white powder from the solution and was collected by filtration. The white powder was washed with ether (5 x 20 mL) and dried under vacuum. Yield: R = H, 76 % (16 g, 37 mmol); R = Me, 85 % (18 g, 40 mmol).

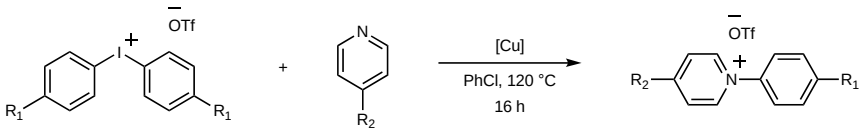

Scheme 2 | Synthesis of aryl-pyridinium triflate salts.

As shown in Scheme 2, in a typical procedure for the synthesis of aryl-pyridinium triflate salts[2], *para*-substituted diaryliodonium triflate salt (2 g, 1 equiv.), Cu(stearate)$_2$ and *para*-substituted pyridine were suspended in PhCl under N_2 in a flame dried round bottom flask charged with a magnetic stir bar. The mixture was heated at 110 °C for 16 h. The solution was cooled down to ambient temperature before the addition of diethylether (10 mL). The precipitate formed was isolated by filtration and was washed with diethylether (3 x 5 mL), acetone (3 x 5 mL). The final product was finally dried under vacuum. Yield: ~85 %.

Molecule 7: ^{1}H NMR (400 MHz, d$_6$-DMSO) δ(ppm) 9.05 (d, $^2J_{H-H}$ = 7.2 Hz, 2H), 8.06 (d, $^2J_{H-H}$ = 7.2 Hz, 2H), 7.68 (d, $^2J_{H-H}$ = 8.3 Hz, 2H), 7.51 (d, $^2J_{H-H}$ = 8.3 Hz, 2H), 2.68 (s, 3H), 2.42 (s, 3H). ^{13}C{^{1}H} NMR (101 MHz, DMSO) δ(ppm): 160.6 (s), 143.7 (s), 141.6 (s), 140.5 (s), 130.1 (s), 128.8 (s), 124.4 (s), 21.9 (s), 21.0 (s).

Molecule 8: ^{1}H NMR (400 MHz, D$_2$O) δ(ppm): 9.55 (d, $^2J_{H-H}$ = 7.7 Hz, 2H), 8.70 (d, $^2J_{H-H}$ = 7.7 Hz, 2H), 7.76 (d, $^2J_{H-H}$ = 8.7 Hz, 2H), 7.55 (d, $^2J_{H-H}$ = 8.7 Hz, 2H), 2.45 (s, 3H). ^{13}C{^{1}H} NMR (101 MHz, D$_2$O) δ(ppm): 147.3 (s), 143.7 (q, $^3J_{C-F}$ = 36.7 Hz), 142.8 (s), 140.5 (s), 131.0 (s), 125.5 (s), 124.8 (s), 120.4 (q, $^1J_{C-F}$ = 107.7 Hz), 21.0 (s).

Molecule 9: ^{1}H NMR (400 MHz, D$_2$O) δ(ppm): 8.87 (d, $^2J_{H-H}$ = 6.3 Hz, 2H), 8.18 (d, $^2J_{H-H}$ = 6.3 Hz, 2H), 7.52 (q, $^2J_{H-H}$ = 8.4 Hz, 2H), 2.44 (s, 3H), 1.43 (s, 9H). ^{13}C{^{1}H} NMR (101

MHz, D_2O) δ(ppm): 172.4 (s), 143.1 (s), 142.2 (s), 139.9 (s), 130.8 (s), 125.2 (s), 123.5 (s), 36.1 (s), 29.0 (s), 20.2 (s).

Molecule 10: ^{1}H NMR (400 MHz, d_6-DMSO) δ(ppm): 8.98 (d, $^{2}J_{H-H}$ = 7.5 Hz, 2H), 7.68 (d, $^{2}J_{H-H}$ = 7.5 Hz, 2H), 7.63 (d, $^{2}J_{H-H}$ = 8.5 Hz, 2H), 7.48 (d, $^{2}J_{H-H}$ = 8.6 Hz, 2H), 4.15 (s, 3H), 2.41 (s, 3H). $^{13}C\{^{1}H\}$ NMR (101 MHz, d_6-DMSO) δ(ppm): 171.7 (s), 146.1 (s), 141.1 (s), 140.1 (s), 130.9 (s), 124.3 (s), 113.8 (s), 58.7 (s), 20.9 (s).

Molecule 11: ^{1}H NMR (400 MHz, D_2O) δ(ppm): 8.13 (d, $^{2}J_{H-H}$ = 8.0 Hz, 2H), 7.37 (q, $^{2}J_{H-H}$ = 6.4 Hz, 4H), 6.94 (d, $^{2}J_{H-H}$ = 8.0 Hz, 2H), 3.22 (s, 6H), 2.37 (s, 3H). $^{13}C\{^{1}H\}$ NMR (101 MHz, D_2O) δ(ppm): 156.3 (s), 140.5 (s), 140.1 (s), 139.5 (s), 130.5 (s), 122.6 (s), 107.6 (s), 39.5 (s), 20.0 (s).

N,N'-(1,4-phenylene)bispyridinium (**12**) was synthesized from slightly modified literature procedures (Scheme 3)[4]:

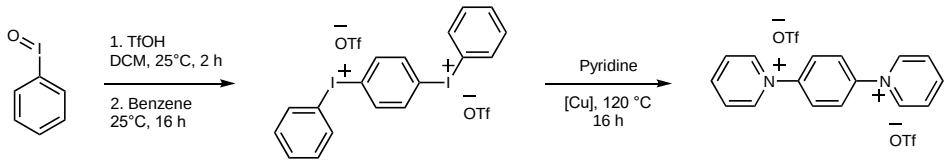

Scheme 3 | Synthesis of N,N'-(1,4-phenylene)bispyridinium.

Iodosobenzene (5 g, 23 mmol, 1 equiv.) was suspended in DCM (50 mL) in a round bottom flask charged with a magnetic stir bar. TfOH (4 mL, 46 mmol, 2 equiv.) was added dropwise yielding an orange solution. After 4 h of stirring at 25 °C, benzene (2 mL, 23 mmol, 1 equiv.) was added. The reaction was stirred for 2 h during which a precipitate was formed. The precipitate was collected by filtration to give a sticky solid. The product was rinsed abundantly with DCM (5 x 20 mL) and diethylether (3 x 10 mL) to afford a white solid which was dried under vacuum. Yield: 34 % (6.4 g, 8.14 mmol).

(*Para*-phenylene)bis(aryliodonium) ditriflate (6 g, 8 mmol, 1 equiv.), and $Cu(stearate)_2$ (150 mg, 0.24 mmol, 0.03 equiv.) were dissolved in anhydrous pyridine (25 mL) in a flame dried round bottom flask charged with a magnetic stir bar under N_2. The brown solution was

heated to reflux for 16 h during which a precipitate was formed. The precipitate was isolated by filtration after cooling down the reaction to ambient temperature. The product was washed with ether (3 x 5 mL) to afford a white solid and dried under vacuum. Yield: 37 % (1.6 g, 3 mmol). Spectroscopic characterization was in agreement with the reported data[4].

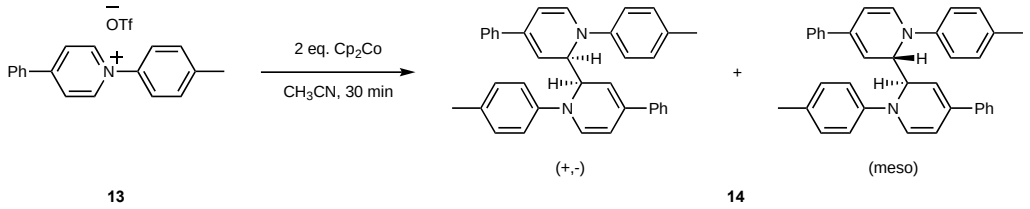

Scheme 4 | Synthesis of 1,1'-ditolyl-2.2'-dihydro-4.4'-diphenyl-2.2'-bipyridine.

As shown in Scheme 4, in a typical procedure for the synthesis of 1,1'-ditolyl-2.2'-dihydro-4.4'-diphenyl-2.2'-bipyridine (**14**), a solution of bis(cyclopentadienyl)cobalt(II) (107.4 mg, 0.57 mmol) in CH_3CN (3 mL) was added to a solution of compound 1-(*p*-Me)C_6H_4-4-phenylpyridinium chloride (**13**, 80 mg, 0.28 mmol) in CH_3CN (2 mL), in a nitrogen glovebox. The homogenous mixture was stirred for 30 min whereafter the solvent was removed under reduced pressure to yield a dark blue solid. The solid was washed with dimethoxyethane (5 x 5 mL) and the yellow crude product (70 mg) was extracted with CH_2Cl_2. Single crystals amenable to X-ray diffraction studies can be grown from diffusion of Et_2O into a CH_2Cl_2 solution. Yield. 35 mg (51%). ^{1}H NMR (300 MHz, CD_2Cl_2, 25 °C): δ = 2.24 (s, 6 H), 5.20 (m, 2 H), 5.54 (m, 1 H), 5.66 (m, 2 H), 5.89 (t, 2 H), 6.66 (d, 2H), 6.84 (d, 1H), 6.98 (m, 7H), 7.27-7.40 (m, 6H), 7.53 (d, 3H). ^{13}C NMR (101 MHz, CD_2Cl_2) δ 144.26, 144.16, 139.82, 139.75, 136.44, 136.12, 131.39, 131.31, 130.68, 130.34, 129.96, 129.82, 128.80, 128.64, 127.79, 127.64, 126.47, 126.38, 117.48, 117.16, 111.93, 109.71, 105.21, 104.81, 56.98, 56.37, 20.58. HRMS (TOF-MS): calcd. for $C_{36}H_{31}N_2$: 491.2465 $[M-H]^+$; found: 491.2487.

Bader charge analysis and density functional theory calculations. The Bader charge was calculated using the Bader Charge Analysis script written by Henkelman and co-workers[6]. All the DFT calculations in this work were carried out with a periodic slab model using the Vienna

ab initio simulation program (VASP)[7-10]. The generalized gradient approximation (GGA) was used with the Perdew-Burke-Ernzerhof (PBE) exchange-correlation functional[11]. The projector-augmented wave (PAW) method[12,13] was utilized to describe the electron-ion interactions, and the cut-off energy for the plane-wave basis set was 450 eV. The D3 correction method by Grimme et al[14] was employed to illustrate the long-range dispersion interactions between the organic molecule, water, and Cu surface. Brillouin zone integration was accomplished using 1×1×1 and 2×2×1 Monkhorst-Pack k-point mesh for organic molecule only and systems with surfaces.

All the adsorption geometries were optimized using a force-based conjugate gradient algorithm. For the modelling of Cu, the crystal structure was optimized, and the equilibrium lattice constants were found to be a_{Cu} = 3.631 Å. For Cu(111), a 4-layer p(6×6) super cell model with 2 upper layers relaxed and 2 lower layers fixed was used. 15 Å vacuum layer was added to all the slab models. The organic molecules are all calculated in 20 Å × 20 Å × 20 Å unit cell to avoid the interaction between the nearby molecules. The reaction mechanism proposed by Goddard and co-workers[15] was used to calculate the entire reaction pathway from CO_2 to C_2H_4. One charged water layer was put on the surface to consider the solvent effect.

Materials characterization. Scanning electron microscopy (SEM) was performed using a Hitachi S-5200. Atomic force microscopy (AFM) measurements were conducted with an Asylum Research Cypher operating in tapping mode. X-ray photoelectron spectroscopy (XPS) measurements were carried out on PHI 5700 ESCA System using Al Kα X-ray radiation (1486.6 eV) for excitation. The powder X-ray diffraction patterns were recorded on Bruker D8 using Cu-Kα radiation (λ = 0.15406 nm). *Operando* hard X-ray absorption spectroscopy (hXAS) measurements were performed at the 9BM beamline of the Advanced Photon Source Advanced Photon Source (APS) located in the Argonne National Laboratory (Lemont, IL). The X-band (9.88 GHz) continuous-wave (CW) electron paramagnetic resonance (EPR) spectra

were recorded on a Bruker (Billerica, MA) EleXsys E500 spectrometer which is equipped with a super-high Q resonator (ER4122SHQE). *In situ* Raman measurements were carried out using a Renishaw inVia Raman Microscope in a modified liquid-electrolyte flow cell and a water immersion objective (63x) with a 785 nm laser, using a 5 s integration and averaging 20 scans per region. The spectra were recorded and processed using the Renishaw WiRE (version 4.4) software. A Ag/AgCl electrode was used as the reference electrode and a Pt wire was used as the counter electrode in all measurements. A graphite rod and 1 M $KHCO_3$ prepared by bubbling CO_2 to 0.5 M K_2CO_3 (99.99%) solution were additionally utilized to rule out the possible influence of electrodeposited metals from either Pt electrode or residual metals in $KHCO_3$[16].

Electrode preparation. The polytetrafluoroethylene (PTFE) electrode was prepared by sputtering 300 nm Cu onto a piece of PTFE membrane (pore size of 450 nm, with polypropylene support on backside) using a pure Cu target (99.99%) at a sputtering rate of 1 Å s^{-1}. The tetrahydro-bipyridine film was electrodeposited onto the PTFE electrode in 0.1 M $KHCO_3$ solution containing 10 mM corresponding additive in a three-electrode setup with PTFE electrode, Ag/AgCl electrode (3 M KCl) and Pt foil being working, reference and counter electrodes, respectively. A constant current of 0.75 mA cm^{-2} was applied on the PTFE electrode (~2 × 2 cm^2 for liquid-electrolyte flow cell, ~3 × 3 cm^2 for MEA) by an Autolab PGSTAT204 (Metrohm-Autolab) for 120 s (the optimum duration. For molecule **12**, 60 s). The additives dimerized through the reactions in Fig. 1a for **1**–**11** and in Fig. 3a for **12** in the main text. After electrodeposition, the electrode was rinsed with DI water, dried by a flow of N_2, and kept in dry environment for further use. For AFM measurement, the additive was electrodeposited on a silicon wafer ((100), 0.001–0.005 ohm cm^{-1}, University Wafer) using the same protocol. In the cases that Cu foil or Cu wire (diameter: 0.202 mm) were used, the additive was electrodeposited using the same protocol. The Cu foil electrodes were electro-polished by

applying a constant voltage of +3 V (*vs.* Cu foil) for 900 seconds in concentrated H_3PO_4 and rinsed with Milli-Q water prior to use.

CO_2RR and product analysis. The CO_2RR measurements were conducted in a gas-tight liquid-electrolyte flow cell or an MEA. The liquid-electrolyte flow cell consists of three compartments: gas chamber, catholyte chamber, and anolyte chamber. The PTFE electrode (with tetrahydro-bipyridine film functionalization) was sandwiched between CO_2 gas chamber and catholyte chamber with an exposure area of 1 cm^2. Catholyte and anolyte chambers were separated by an anion-exchange membrane (Fumapem FAA-3-PK-130). An Autolab PGSTAT204 in a potentiostatic mode was used as electrochemical workstation. The PTFE electrode, Ag/AgCl electrode (3 M KCl), and Ni foam (geometric area ~2 cm^2) were employed as working, reference and counter electrodes, respectively. The applied potentials were converted to the reversible hydrogen electrode (RHE) scale with iR correction through the following equation:

$$E_{RHE} = E_{vs\ Ag/AgCl} + 0.059 \times pH + 0.210 + iR$$

where i is the current at each applied potential and R (10.4 ohm) is the equivalent series resistance measured via electrochemical impedance spectroscopy (EIS) in the frequency range of 10^5 – 0.1 Hz with an amplitude of 10 mV.

Aqueous $KHCO_3$ electrolyte (1 M, saturated with CO_2) was used as both catholyte and anolyte and was circulated through the flow cell using peristaltic pumps with a silicone Shore A50 tubing. The electrolyte was bubbled with CO_2 during the entire electrolysis process. The electrolyte flow rate was kept at 10 mL min^{-1}. The flow rate of the CO_2 gas flowing into the gas chamber was kept at 50 standard cubic centimeters per minute (sccm) by a digital gas flow controller.

The MEA is a complete 5 cm^2 CO_2 electrolyzer (Dioxide Materials) which includes a titanium anode flow field, 904 L Stainless Steel cathode flow field and associated nuts, bolts

and insulating kit. The PTFE electrode was attached on the cathode by copper tape at the edge of the electrode to electrically connect it with the cathode. The Cu side of the PTFE electrode faced outside. The copper tape was protected by Kapton tapes to avoid electrical contact with membranes or electrolytes. A Sustainion® membrane (Dioxide Materials) was activated in 1 M aqueous KOH solution for 24 hours, washed with water and used as the anion-exchange membrane. The anode consisted of iridium oxide supported on titanium mesh (IrO_x/Ti mesh) was prepared by a dip coating and thermal decomposition method[17]. A Ti mesh was dip coated into an isopropanol solution containing (10%, v/v) concentrated HCl and $IrCl_3 \cdot xH_2O$ (3 mg mL^{-1}), dried at 100 °C for 10 minutes and calcinated at 500 °C for 10 minutes in air. The procedure was repeated for a few times to increase the loading of iridium. The MEA was assembled in a way as illustrated in Supplementary Figs. 27 and 28. An Autolab PGSTAT204 in a potentiostatic mode with a current booster (10 A) was used as electrochemical workstation to apply voltage to the cathode and anode. No *i*R compensation was applied. Aqueous $KHCO_3$ electrolyte (0.1 M) was used as the anolyte and was circulated using a peristaltic pump with a robust soft PVC tubing (McMaster-Carr, 5231k134). The electrolyte flow rate was kept at 10 mL min^{-1}. The flow rate of the CO_2 gas flowing into the gas chamber was kept at 80 sccm by a digital gas flow controller. CO_2 was then flowed through a humidifier (7/8 full of Milli-Q water, room temperature) prior to the MEA. The full-cell voltage was gradually increased from 3 V to 3.65 V and then kept constant over the electrolysis course.

The gaseous products were analyzed by gas chromatography (PerkinElmer Clarus 600) equipped with a thermal conductivity detector (TCD) and a flame ionization detector (FID). High purity Argon (99.99%) was used as the carrier. Liquid products were quantified by ^1H NMR spectroscopy (600 MHz Agilent DD2 NMR Spectrometer) using dimethyl sulfoxide (DMSO) as the internal standard.

Local species concentration modelling. The local concentrations of $CO_{2,aq}$, CO_3^{2-}, HCO_3^-, and OH^- in an electrolyte solution under CO_2RR conditions were modelled in COMSOL 5.3a (COMSOL Multiphysics, Stockholm, Sweden) using the Transport of Dilute Species physics in a one-dimensional domain. This model is based on previous paper[18] and accounts for $CO_{2,aq}$, CO_3^{2-}, HCO_3^-, and OH^- evolution as $CO_{2,aq}$ is reduced via electrocatalysis in either K_2CO_3 or $KHCO_3$. A time-dependent study is performed to simulate species evolution away from the interface. At the left boundary, the gas-catalyst-electrolyte interface, the $CO_{2,aq}$ concentration is specified according to Henry's Law and the Sechenov effect, with zero flux imposed for CO_3^{2-}, HCO_3^-, and OH^-. The right boundary concentrations are fixed at the bulk values for the given electrolyte. To model CO_2RR, a 300 nm catalyst layer is imposed over which the $CO_{2,aq}$ is reduced and OH^- is produced according to the reactions:

$$R_{CO_2} = \frac{[CO_2]_{aq}}{[CO_2]_{aq,0}} \frac{j}{F} \frac{\epsilon}{L_{cat}} \frac{\sum FE_{CO_2RR}}{ne_{CO_2RR}}$$

$$R_{OH} = \frac{j}{F} \frac{\epsilon}{L_{cat}}$$

where $[CO_2]_{aq,0}$ is the equilibrium saturation $CO_{2,aq}$ concentration in the bulk electrolyte, j is the current density applied, F is Faraday's constant, ϵ is the catalyst porosity (0.6), and L_{cat} is the size of the catalyst layer, FE_{CO_2RR} is the Faradaic efficiency of a given product of CO_2 reduction (based on experimental observations), and ne_{CO_2RR} are the number of electrons required for the reduction reaction. The diffusion-reaction equations are found in the previous works[18,19] with diffusion constants of $D_{CO_2}=1.91\cdot10^{-9}$ m^2s^{-1}, $D_{OH^-}=5.27\cdot10^{-9}$ m^2s^{-1}, $D_{HCO_3^-}=1.19\cdot10^{-9}$ m^2s^{-1}, and $D_{CO_3^{2-}}=0.923\cdot10^{-9}$ m^2s^{-1}(ref [20]).

XAS fitting. An IFEFFIT package was used to analyze the hXAS spectra[21,22]. Standard data-processing including energy calibration and spectral normalization of the raw spectra was performed using Athena software. To extract the Cu bonding information, a Fourier transform was applied to convert the hXAS spectra from an energy space to a radial distance space. Then,

a standard fitting analysis of the first shell between 1.6 and 3.0 Å was carried out using Artemis software. The phase and amplitude functions of Cu-Cu was calculated with FEFF; S0/σ2 values of 0.89/0.00825 for Cu was determined from Cu foil, which was then applied to the Cu hXAS fitting.

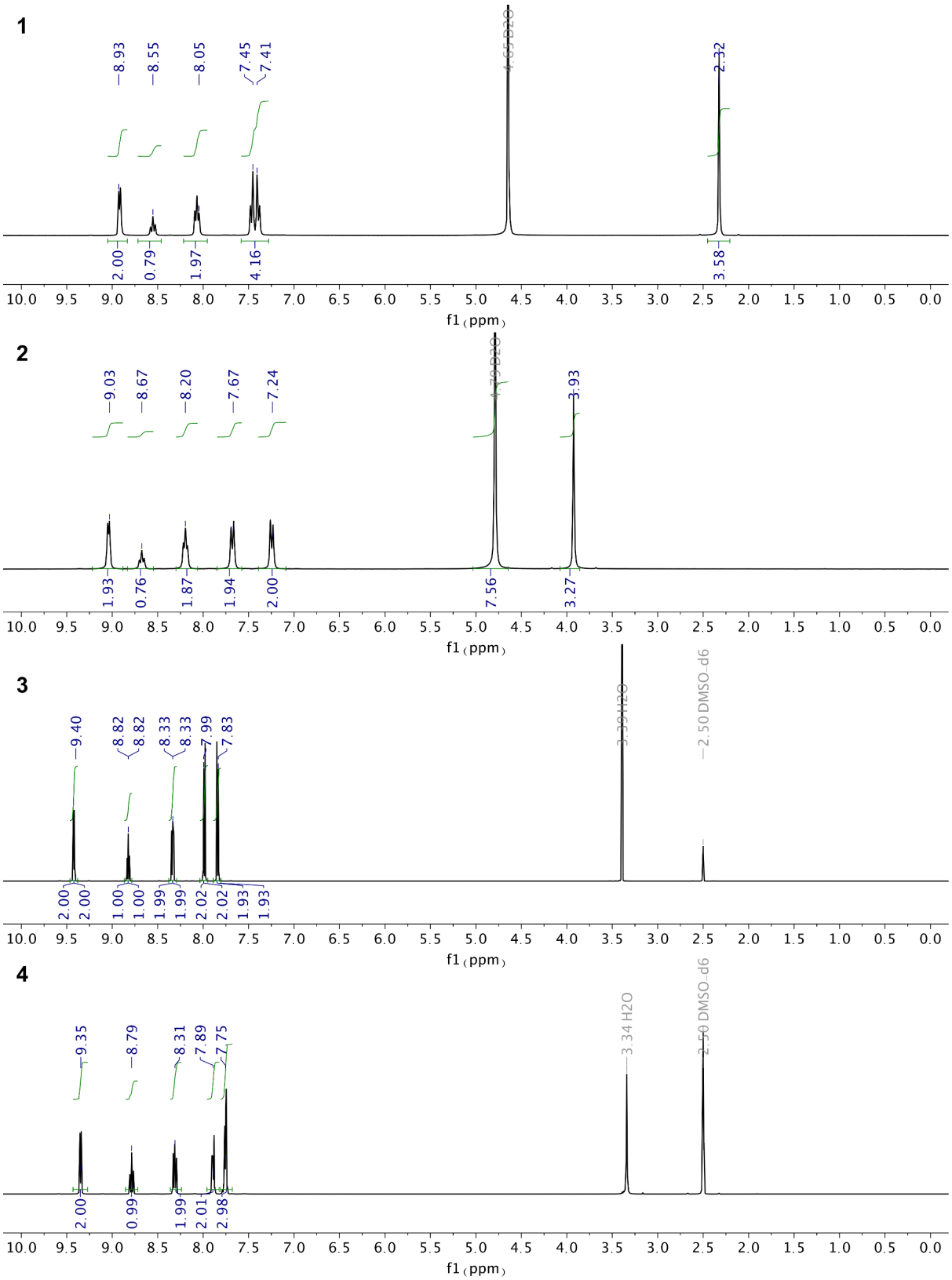

Supplementary Fig. 1 | ^{1}H NMR of the molecules 1–4. The spectra of **1** and **2** were recorded in D_2O (298 K) and the rest in DMSO-*d*$_6$ (298 K).

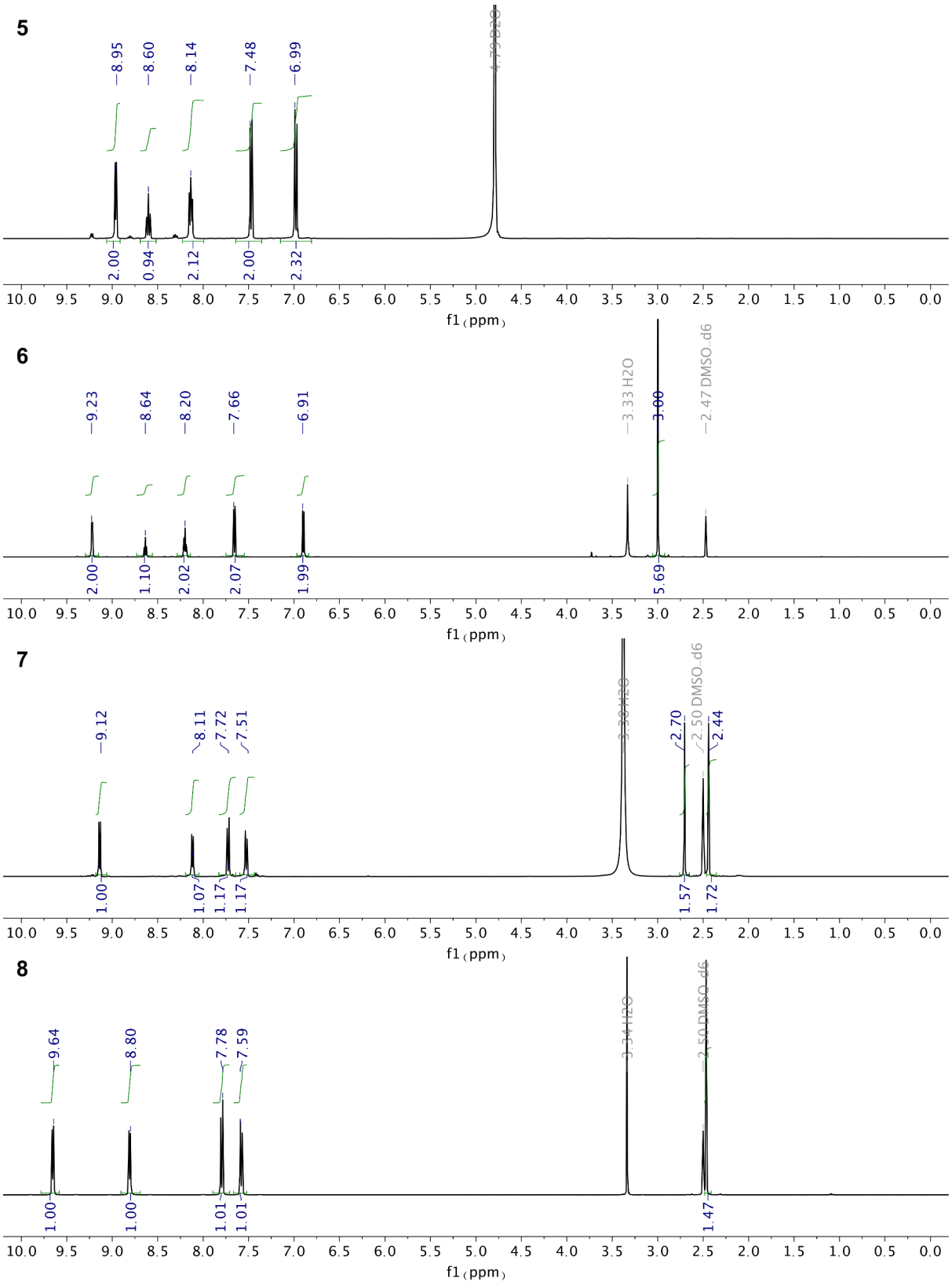

Supplementary Fig. 1 (cont.) | ^{1}H NMR of the molecules 5–8. The spectrum of **5** was recorded in D_2O (298 K) and the rest in DMSO-d_6 (298 K).

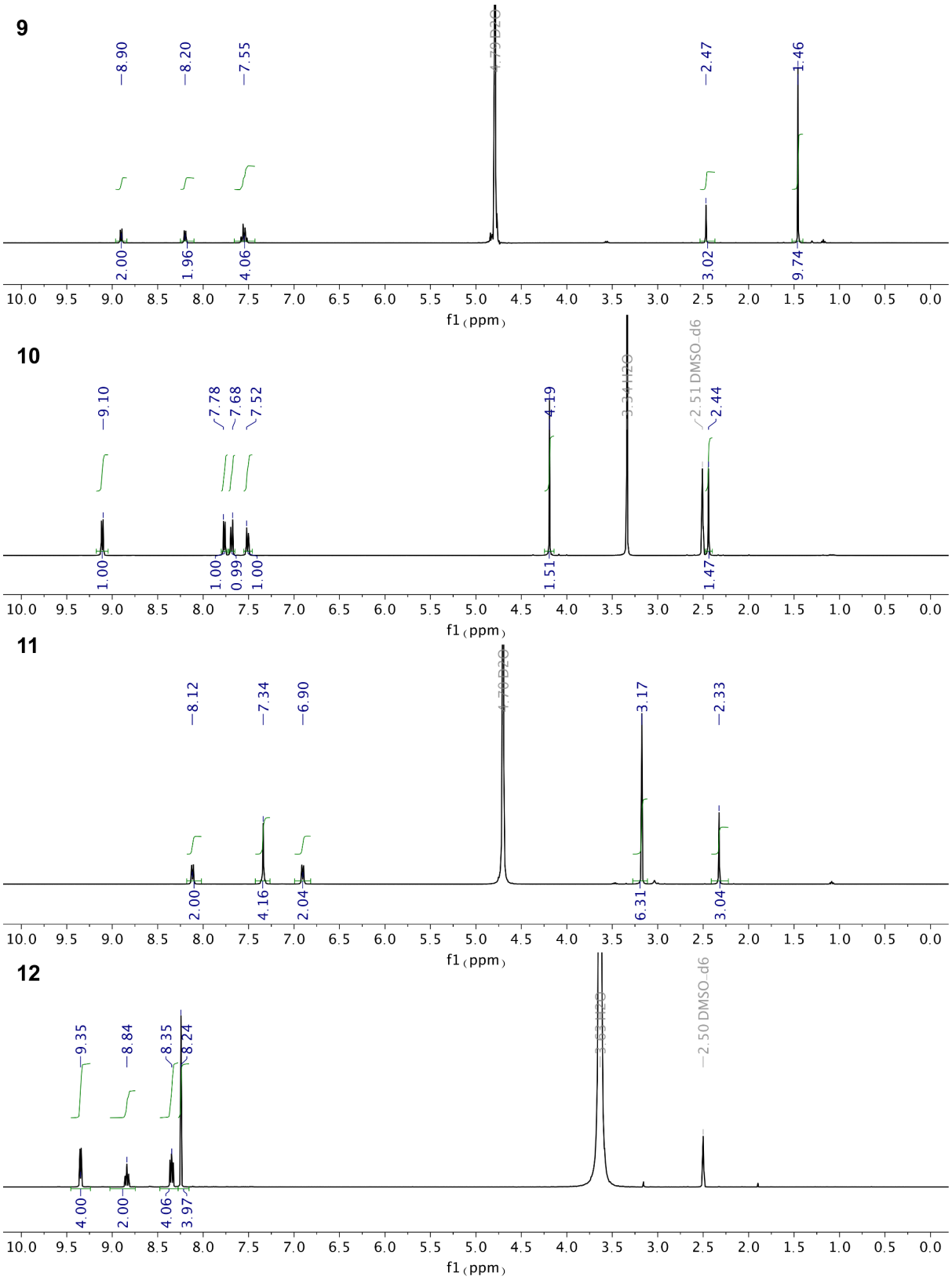

Supplementary Fig. 1 (cont.) | ^{1}H NMR of the molecules 9–12. The spectra of **9** and **11** were recorded in D_2O (298 K) and the rest in DMSO-d_6 (298 K).

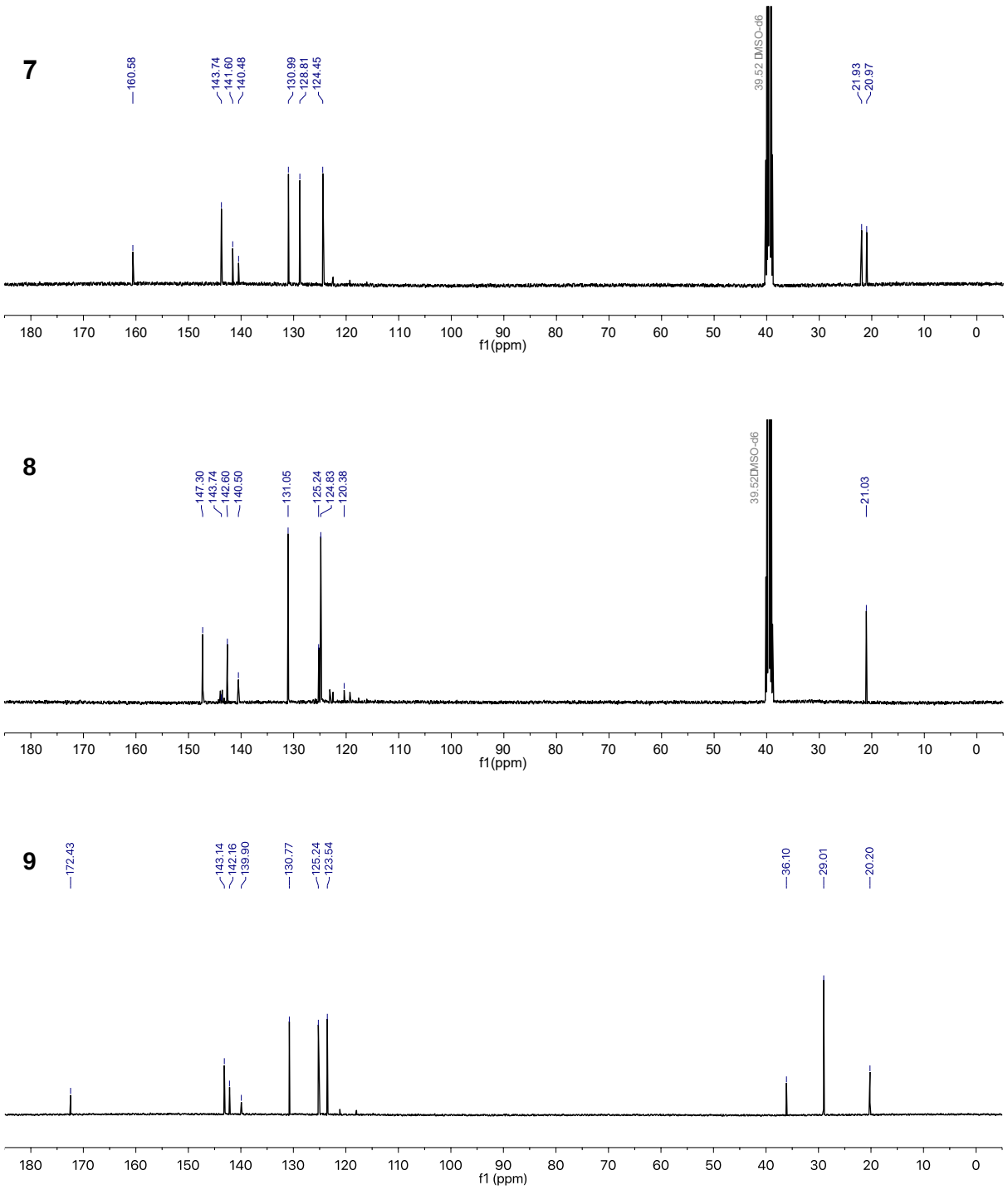

Supplementary Fig. 2 | ^{13}C NMR of the new molecules 7–9. The spectrum of the molecule **9** was recorded in D_2O (298 K) and the rest in DMSO-d_6 (298 K).

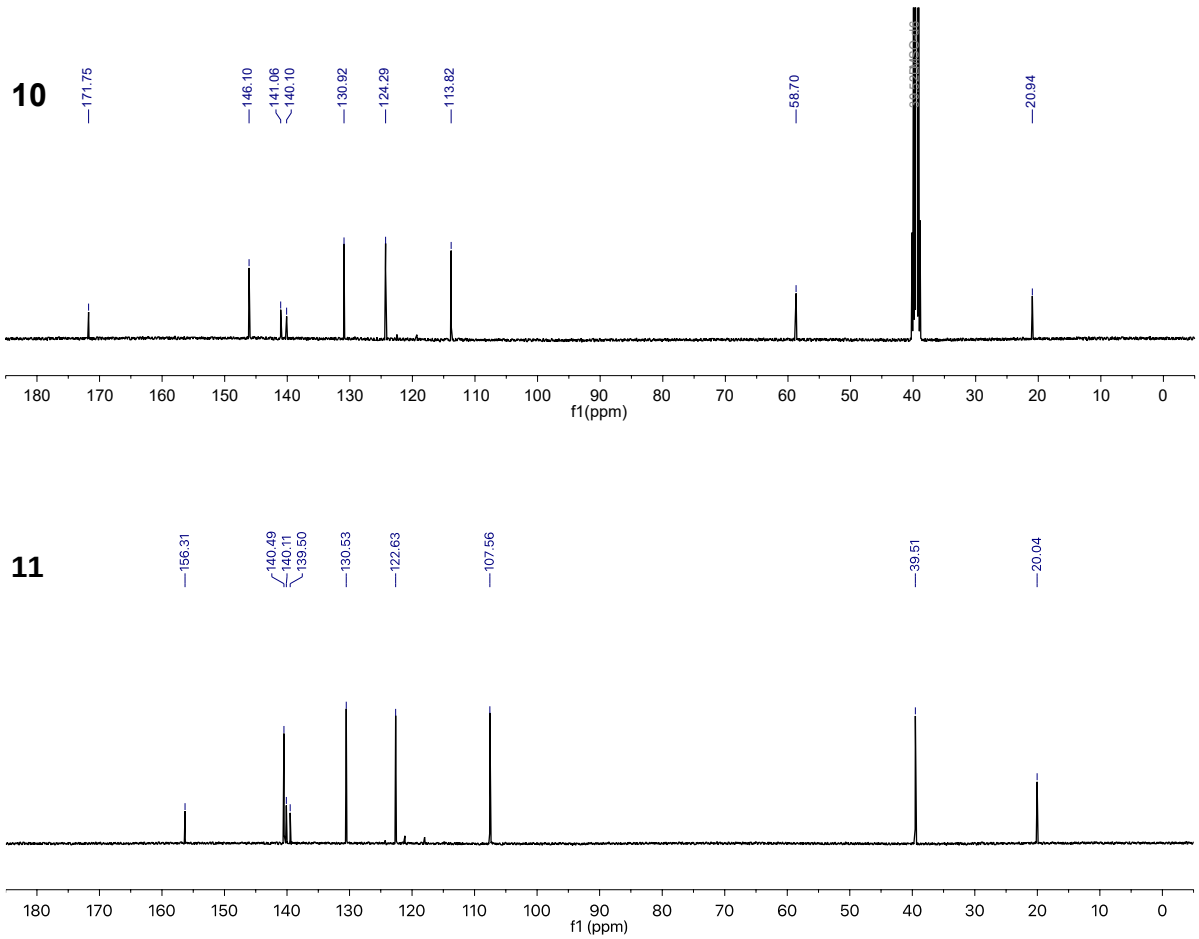

Supplementary Fig. 2 (cont.) | ^{13}C NMR of the new molecules 10 and 11. The spectrum of the molecule **10** was recorded in DMSO-d_6 (298 K) and **11** in D_2O (298 K).

Supplementary Note 1 | Quantification of the *para,para*:*ortho,ortho* ratios of the organic *N*-aryl-substituted tetrahydro-bipyridines. An example of a *para,para*-coupled tetrahydro-bipyridine has been reported and spetroscopically characterized previously[1]. For the additives used in this study, coupling in both *ortho* and *para* positions is possible, potentially resulting in multiple constitutional isomers and stereoisomers. To firmly establish that an *ortho,ortho*-coupling mechanism is possible during the dimerization of the pyridinium additives, a chemical reduction experiment of a *para*-substituted pyridinium model compound (**13**) was carried out. Since the *para* position of such an additive is blocked by a phenyl group, a preferential *ortho,ortho*-coupled tetrahydro-bipyridine (**14**) was formed, as confirmed by a single-crystal X-ray diffraction study (Supplementary Fig. 3). The resulting ^{1}H NMR spectrum (Supplementary Fig. 4) is expectedly complicated due to the generation of a mixture of stereoisomers.

The ^{1}H NMR spectra (Supplementary Fig. 5) of the film deposited from **1**–**11** at the surface of a Cu foil electrode suggest that all the films are principally made of two components, with the spectra being complicated by the presence of constitutional isomers and stereoisomers resulting from *ortho,ortho*-coupling, *ortho,para*-coupling, and minor organic byproducts. In most cases, the major component corresponds to the *para,para*-coupled product, with the minor component to the *ortho,ortho*-coupled product (labeled in blue or in grey with a *, respectively). The percentage of *para,para*-tetrahydro-bipyridine in the mixture could be quantified in most cases from the specific multiplicity of the resonances between 6 and 6.5 ppm (doublet *vs.* doublet of triplets, respectively). In both cases these protons have been assigned to the *ortho*-pyridinium ring, corresponding to two and one proton, respectively. The percentage was quantified from the following equation:

$$\text{Percentage}_{para} = \frac{\text{integral (doublet/2)}}{\text{integral (doublet of triple)} + \text{integral (doublet/2)}} \times 100\%$$

In some cases, some remaining unreacted pyridinium additive precursor are also present in the ^{1}H NMR spectra and are labeled in grey (without a *). This is most likely because the film was not rinsed with sufficient water prior extraction. The ^{1}H NMR spectra of the organic films from additives **2**, **7**, **9** and **10** could not be assigned due to the complexity of the spectra and the low amount of precipitate collected on the Cu electrode, and therefore the ratio could not be determined. The percentage was summarized below:

Molecule	percentage *para,para isomer* in tetrahydro-bipyridines
1	85%
3	55%
4	73%
5	100%
6	61%
8	100%
11	100%

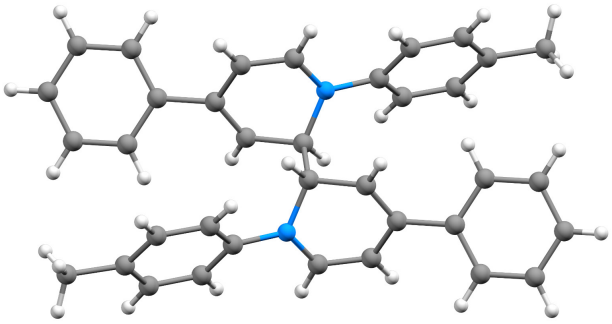

Supplementary Fig. 3 | Single-crystal X-ray structure of compound 14. Carbon atoms are depicted in gray, nitrogen in blue, and hydrogen in white.

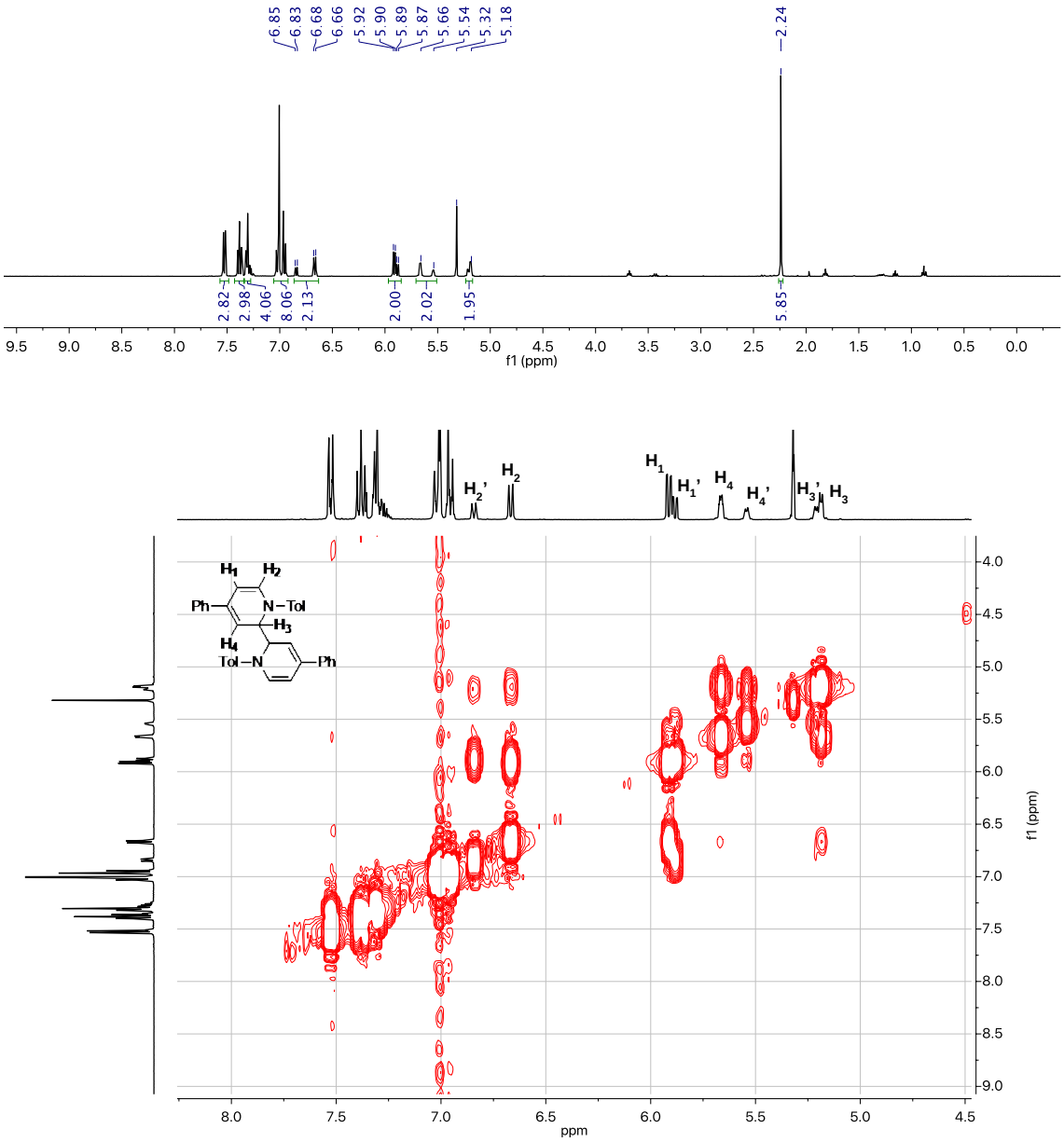

Supplementary Fig. 4 | ^{1}H NMR and COSY spectra of compound 14. The spectra were recorded in CD_2Cl_2 (298 K).

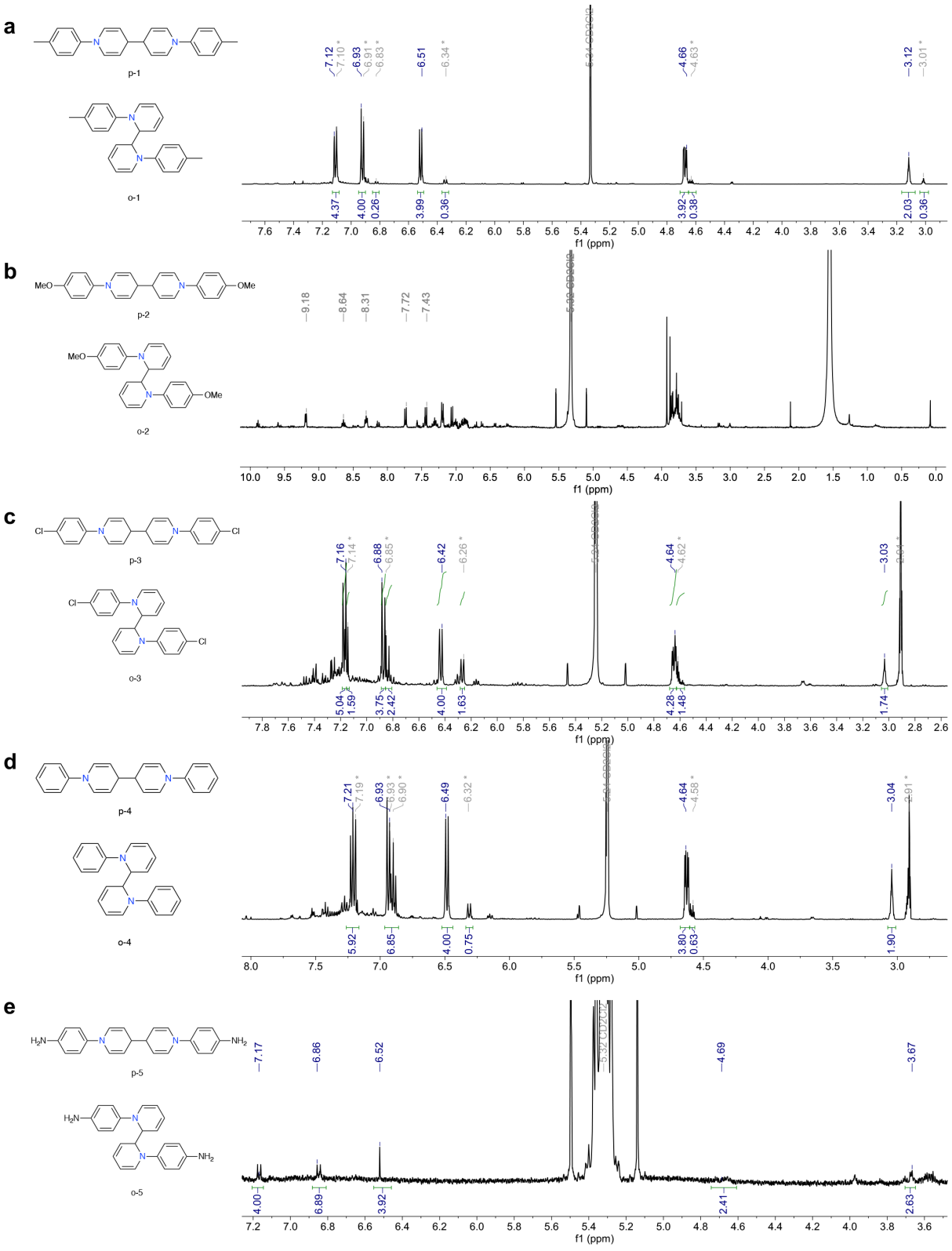

Supplementary Fig. 5 | Molecular structures and ^{1}H NMR spectra of *N*-aryl-substituted tetrahydro-bipyridines formed from additives 1–5. The ^{1}H NMR spectrum of the tetrahydro-bipyridine from additive **2** could not be assigned.

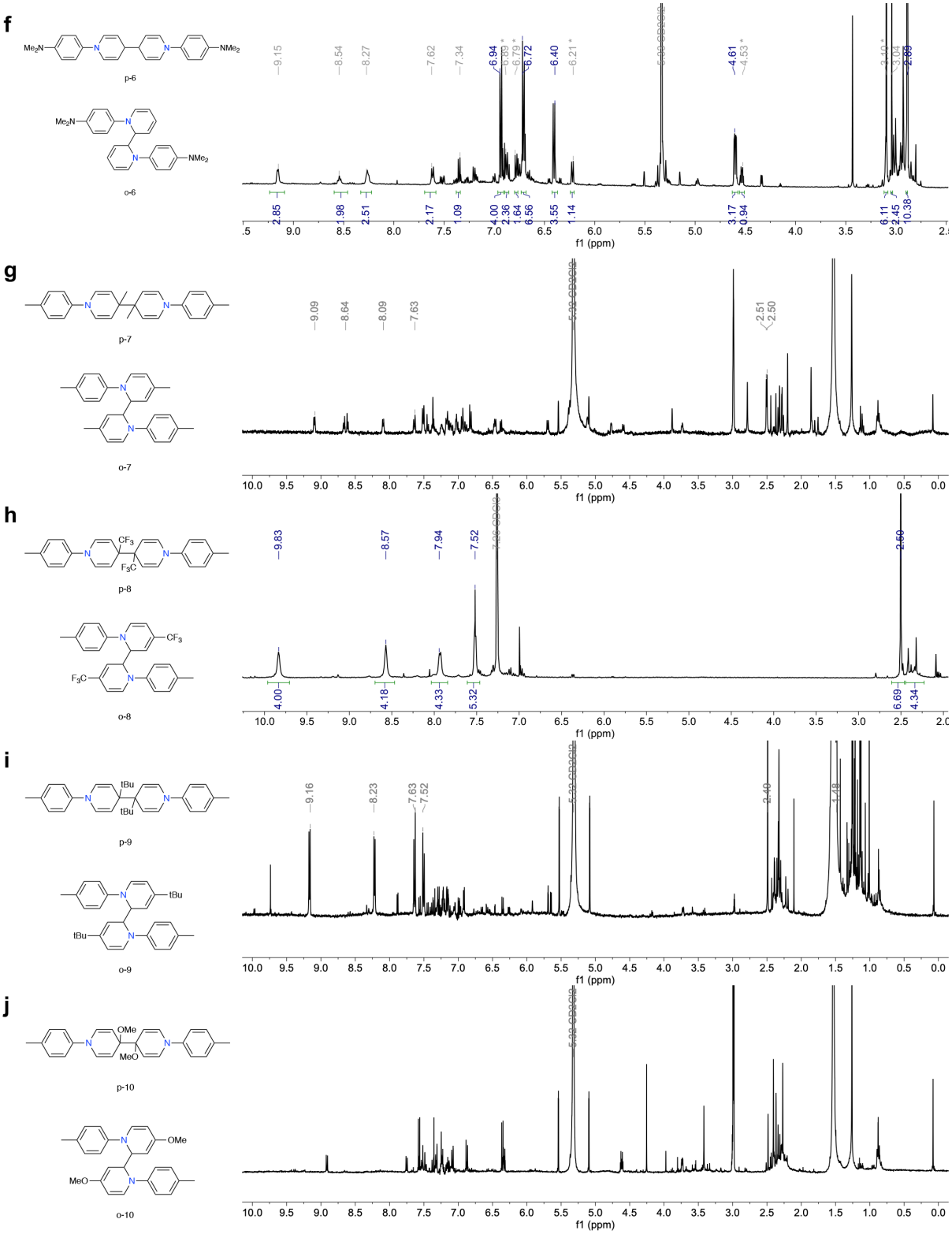

Supplementary Fig. 5 (cont.) | Molecular structures and ^{1}H NMR spectra of the *N*-aryl-substituted tetrahydro-bipyridines formed from additives 6–10. The ^{1}H NMR spectra of the tetrahydro-bipyridines from additives **7**, **9** and **10** could not be assigned.

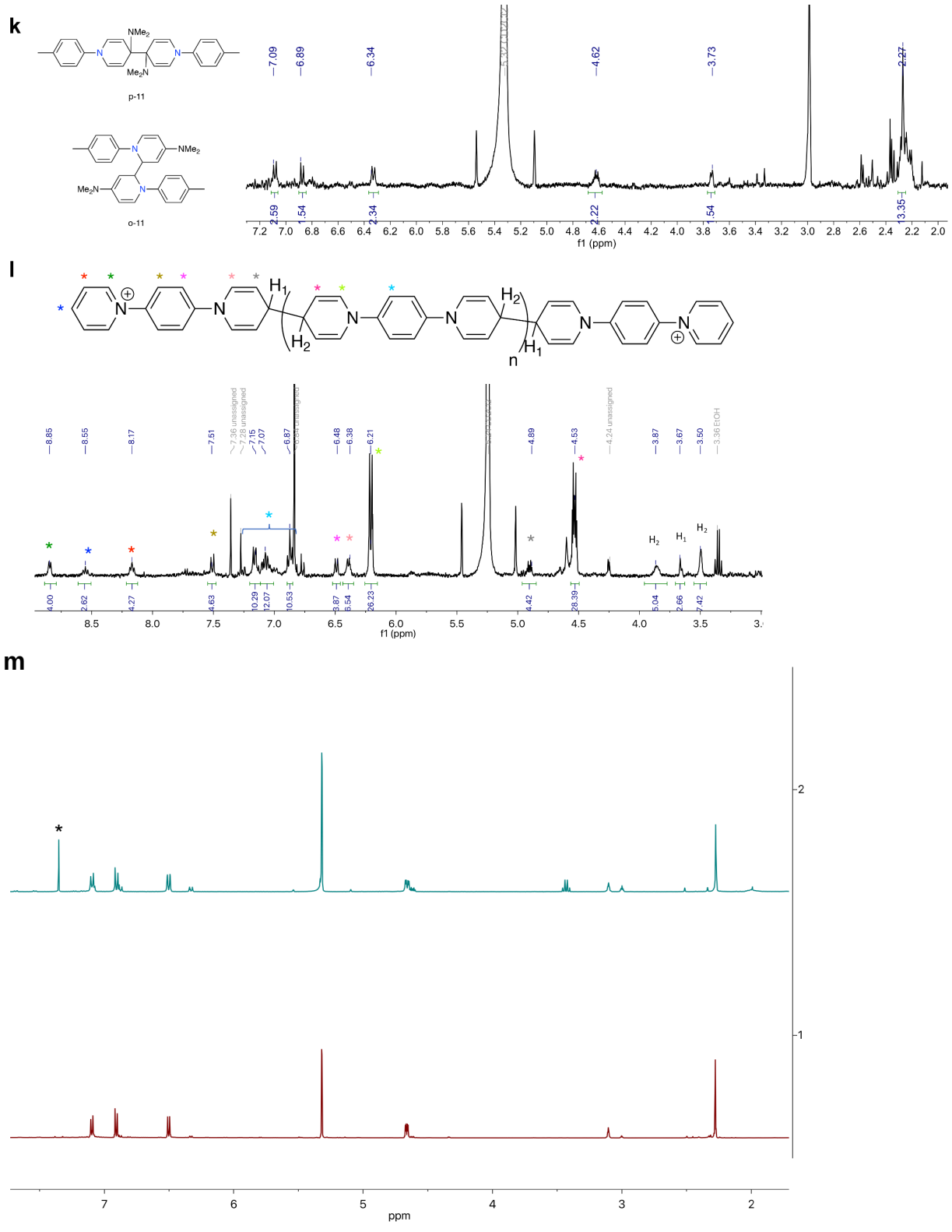

Supplementary Fig. 5 (cont.) | Molecular structures and ^{1}H NMR spectra of the *N*-aryl-substituted tetrahydro-bipyridine and oligomer formed from additives 11 and 12. All the spectra were recorded in CD_2Cl_2 except the film from molecule **8** which was recorded in $CDCl_3$ (298 K)[1]. Panel **l**, ^{1}H NMR spectrum zoomed in the region of interest of the oligomer formed

from molecule **12** in CD_2Cl_2. The spectrum suggests that the film deposited on the Cu electrode consists of an oligomer. The two end groups consist of 1-(1-4dihydropyridine)phenyl-4-pyridinium moieties and the repeating unit of a 1-4-di(1-4dihydropyridine)phenyl block. From the ratio between the numbers of protons of the two end groups and the repeating units (accounted for 28 protons and 84 protons, respectively) the number of repeating units was found to be three. Therefore, the oligomer deposited on the Cu appears to result primarily from the reductive coupling of five N,N'-(1,4-phenylene)bispyridinium additive (**12**). To prepare sufficient quantities of film for NMR characterization (**a**–**l**), longer electrodeposition time at a fixed applied potential (-1 V *vs.* RHE) on a copper foil electrode was adopted. Panel **m**: In order to evaluate if the chemical composition of the film prepared by this method was the same as the one prepared for electrocatalysis measurement, we compared the ^{1}H NMR spectra of films formed from additive **1** prepared by both methods (*top* for fixed applied potential on copper foil, *bottom* for fixed current on electrode described in Electrode Preparation part in Methods). The spectra are very similar, indicating the films prepared by both methods have similar composition. * denotes signal from benzene contamination.

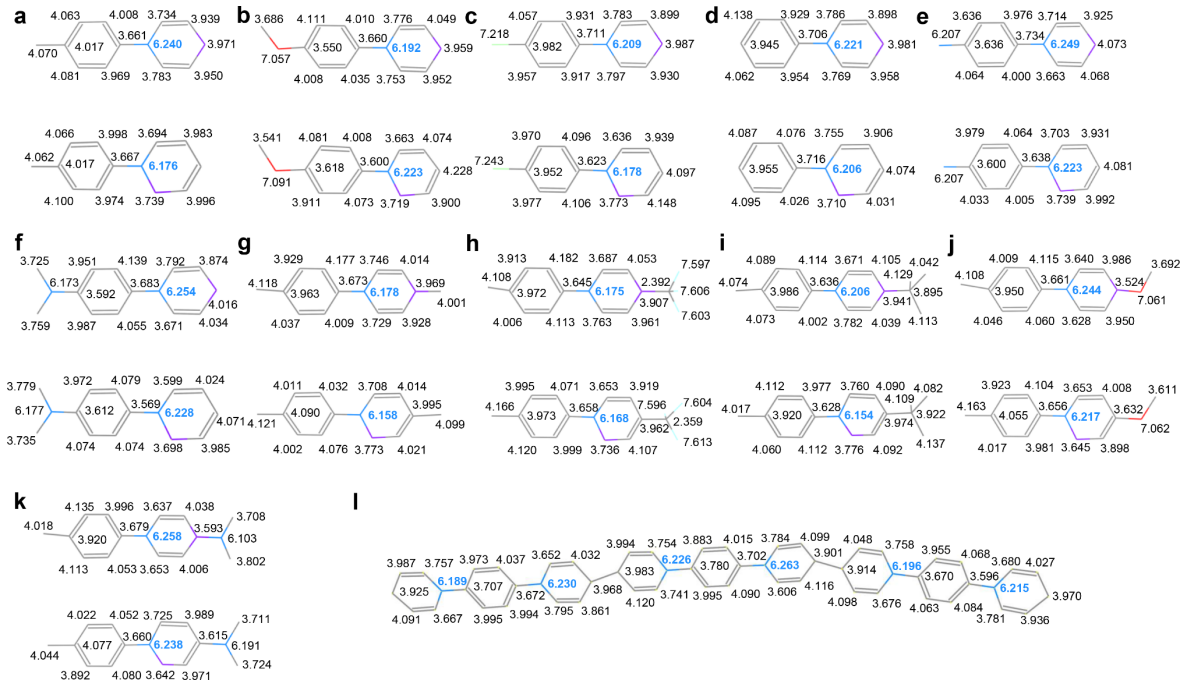

Supplementary Fig. 6 | Formal Bader charges of the *N*-aryl-substituted tetrahydro-bipyridines and the *N*-aryl-dihydropyridine-based oligomer formed from molecule 1–12. Due to the symmetric molecular structure of the tetrahydro-bipyridines, we used a hydrogen atom to replace half of the tetrahydro-bipyridine unit. The position of carbon atom with this hydrogen atom was labelled in purple. The oligomer was calculated as resulting from three units of initial additive. The hydrogen atoms and corresponding formal Bader charges were not shown to keep the values of interest easy to read. The Bader charge of an atom is calculated by subtraction of the formal Bader charges from the outermost electron number of the atom (1, 4, 5, 6, 7 and 7 for H, C, N, O, Cl and F, respectively). Taking nitrogen atom in **a** as an example: The Bader charge is 5 – 6.240 = -1.240. The Bader charge of nitrogen atom of tetrahydro-bipyridines was calculated by averaging the charges in the *ortho,ortho* and the *para,para* tetrahydro-bipyridines in cases where their ratio could be determined from ^{1}H NMR data (Supplementary Fig. 6) using the following equation:

$$\text{Bader charge of } N_{average} = \text{Bader charge}_{para} \times \text{percentage}_{para} + \text{Bader charge}_{ortho} \times (1 - \text{percentage}_{para})$$

The Bader charge of nitrogen atom in the oligomer was calculated by averaging the charges of all the six nitrogen atoms.

Supplementary Note 2 | Influence of the *N*-aryl-substituted tetrahydro-bipyridines on Cu electrodes. As seen in the SEM images (Supplementary Fig. 7a,b), the modification of the *N*-aryl-substituted tetrahydro-bipyridine dimerized from **1** did not change the morphology of Cu. The thickness of the as-formed film is about 10 nm (Supplementary Fig. 7c,d). The modification also did not change the crystallinity of Cu substrate based on XRD characterization (Supplementary Fig. 7e). Contact angle measurement on each tetrahydro-bipyridine-functionalized Cu electrode showed that the modification did not significantly affect the wettability of Cu surface. Further, no trend for the wettability of the electrode surface and ethylene selectivity (Supplementary Fig. 7f) was found.

The influence of the *N*-aryl-substituted tetrahydro-bipyridine film on the local environment near the active Cu surface and transport properties of reactants and ions were further studied. The linear sweep voltammetry (LSV) curves of Cu and Cu-**1** showed no difference at the normal hydrogen electrode (NHE) scale under either N_2 (Supplementary Fig. 8a) or CO_2 (Supplementary Fig. 8b) atmospheres. This indicates that the local pH near the Cu surface is similar in cases with or without the modification of the *N*-aryl-substituted tetrahydro-bipyridines, i.e., the as-formed films does not create a highly alkaline environment near the active Cu surface, since the water reduction reaction is pH-dependent at the NHE scale. This also indicates that the transport of water and CO_2 is not limited because a mass-transport limited current was not seen.

To further explore the transport of water through the *N*-aryl-substituted tetrahydro-bipyridine film, Cu-**1** was electro-oxidized with ^{18}O labeled water ($H_2{}^{18}O$) or unlabeled water ($H_2{}^{16}O$) via the following equation:

$$2Cu + H_2O \rightarrow Cu_2O + 2e^- + 2H^+$$

The Raman spectrum shows a red shift on the as-formed $Cu_2{}^{18}O$ sample compared to that on the $Cu_2{}^{16}O$ sample (Supplementary Fig. 8c), in agreement with the previous report[23]. This result confirms that water can penetrate the molecular coating layer to reach the Cu surface.

OH^- adsorption was used to study whether the *N*-aryl-substituted tetrahydro-bipyridines affect the exposed crystal facets of Cu surface, where the CO_2RR takes place (Supplementary Fig. 8d). Three peaks were identified to associate with the OH^- adsorption on Cu(100), Cu(110) and Cu(111)[24]. Their ratios on bare Cu and Cu-**1** were quantified by integrating the charges of each peak. The values are 69:1.7:29 and 65:1.5:34, respectively. The similar ratios indicate that the deposited molecular layers do not change or selectively cover crystal orientations on Cu surfaces. Moreover, the OH^- adsorption peaks on Cu and Cu-**1** are at the same position, further confirming that pH near the Cu surface is the same with or without the modification of the tetrahydro-bipyridine dimerized from **1** because the OH^- adsorption behavior is local pH-dependent[25].

To study a possible interaction between the terminal amine moieties in tetrahydro-bipyridines formed from **5**, **6**, and **11** with CO_2, we synthesized the corresponding dimeric species of the additives and they were exposed to isotopic labeled $^{13}CO_2$. Since additives **6** and **11** contain a more nucleophilic nitrogen atom (tertiary amine) compared to **5** (primary), we decided to investigate the reactivity of these two additives. Examination of the ^{13}C NMR spectra of the reaction mixture after exposure with $^{13}CO_2$ (Supplementary Figs. 9 and 10) rule out any involvement of the terminal amine moieties in the activation of CO_2 to form any carbamate species[26] (spectra do not show any intense resonances in the region of 160-180 ppm). This result suggests that these terminal amines do not interact with CO_2 molecules, which may affect the diffusion properties of CO_2 or provide additional binding sites for CO_2 or intermediates in the CO_2RR[27]. The result also suggests that it is safe to keep additive **5**, **6** and **11** in the Bader charge analysis and the correlation in Fig. 1 in the main text is retained.

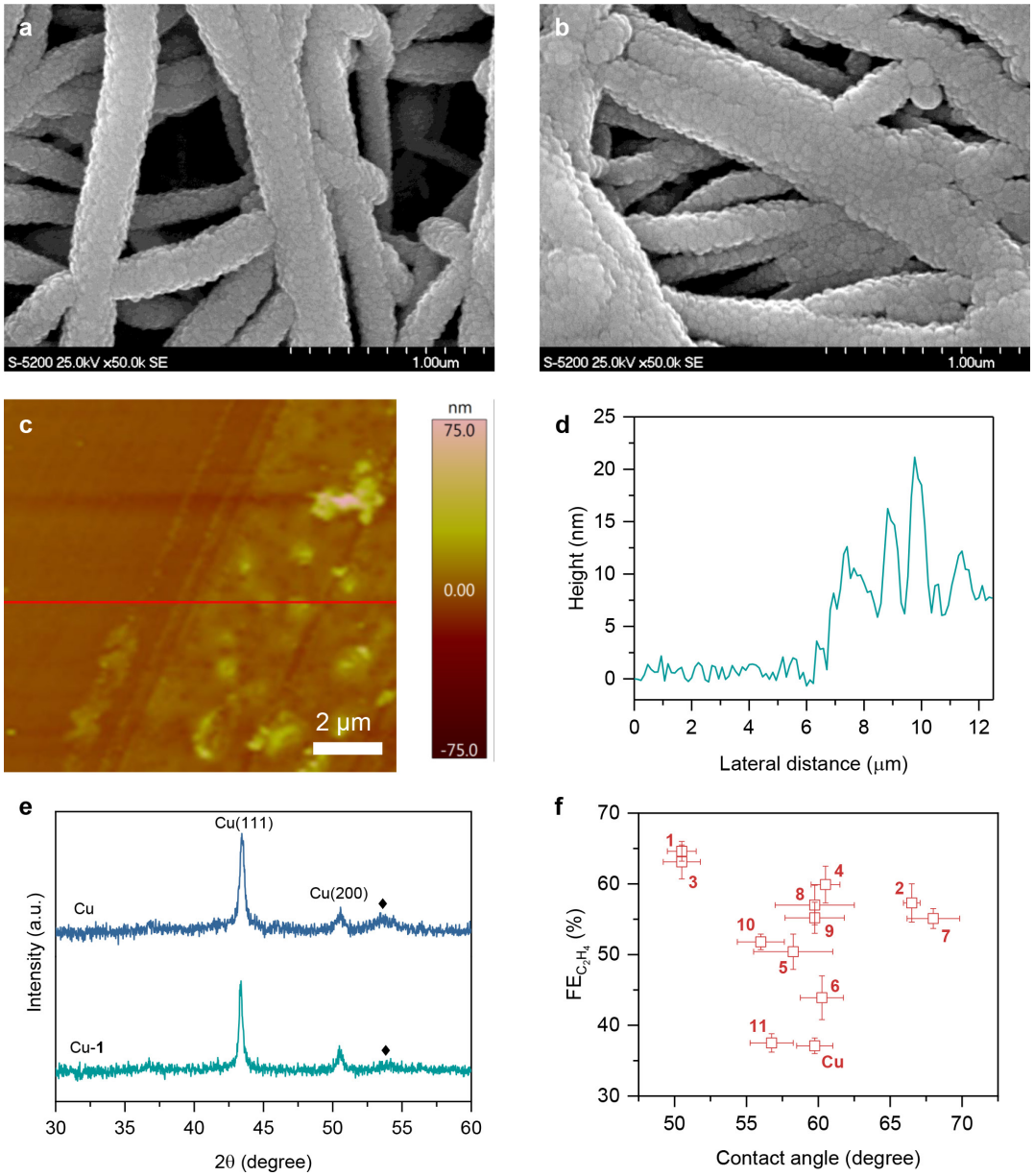

Supplementary Fig. 7 | Characterizations of tetrahydro-bipyridine modified Cu electrode. SEM before (**a**) and after (**b**) modification of *N*-aryl-substituted tetrahydro-bipyridine formed from **1** on PTFE electrode sputtered with 300 nm Cu. AFM (**c**) and corresponding height profile (**d**) of the film electrodeposited from **1** on a silicon wafer. **e**, XRD patterns before and after modification of the tetrahydro-bipyridine formed from **1** on the electrode. The peak labeled by ♦ belongs to PTFE substrate. **f**, Contact angles on bare Cu and Cu modified by tetrahydro-bipyridines formed from **1**–**11**. The values are at the range of 40 – 60 degree.

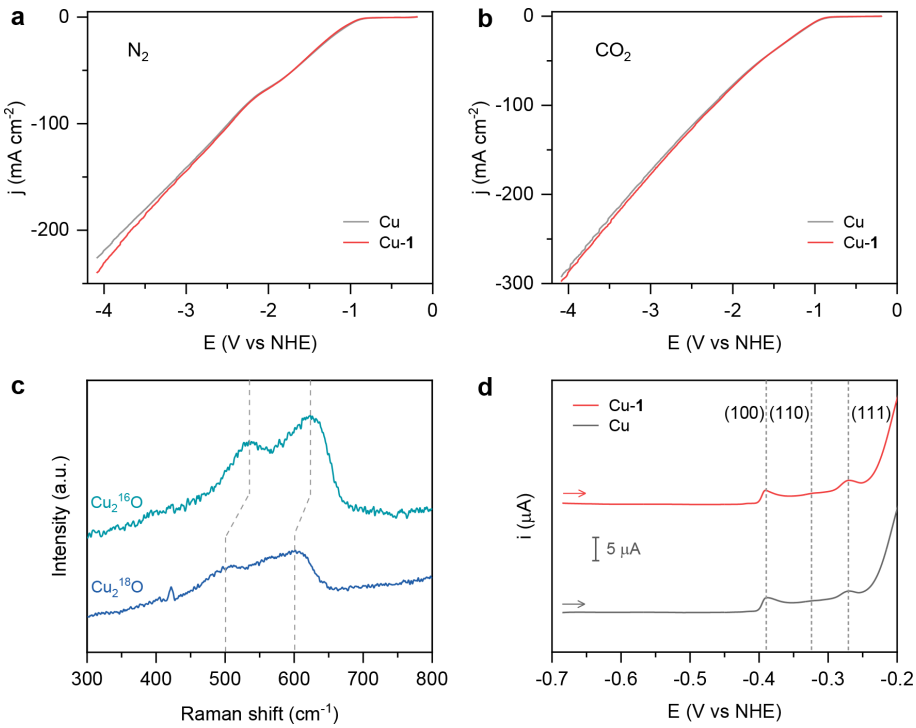

Supplementary Fig. 8 | Transport properties of reactants and ions and local environment near active Cu surface. Linear sweep voltammetry curves of Cu and Cu-**1** electrodes in a liquid-electrolyte flow cell using 1 M $KHCO_3$ as electrolyte. N_2 (**a**) or CO_2 (**b**) was flowed through the gas chamber. The electrolytes were stopped flowing during measurements. **c**, Raman spectra of Cu_2O formed from electrochemical oxidation of Cu-**1** by sweeping the potential from -0.6 V to +0.2 V vs Ag/AgCl at a scan rate of 20 mV s^{-1} in 0.1 M $KHCO_3$ solution (containing 35 mM KCl) saturated with N_2. The electrolytes were prepared using ^{18}O labeled water ($H_2{}^{18}O$) or unlabeled water ($H_2{}^{16}O$), respectively. **d**, OH^- adsorption curves of Cu and Cu-**1** electrodes in 0.1 M KOH solution saturated with N_2.

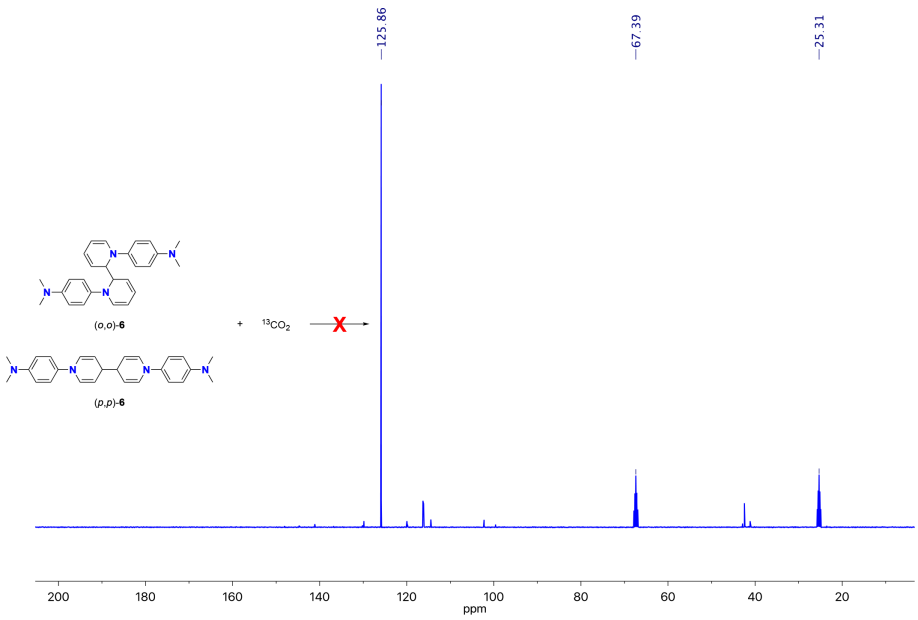

Supplementary Fig. 9 | ^{13}C NMR spectrum of the species after the reaction between $^{13}CO_2$ and tetrahydro-bipyridine dimerized from 6. Peak at 125.86 ppm corresponds to dissolved $^{13}CO_2$ in the reaction mixture.

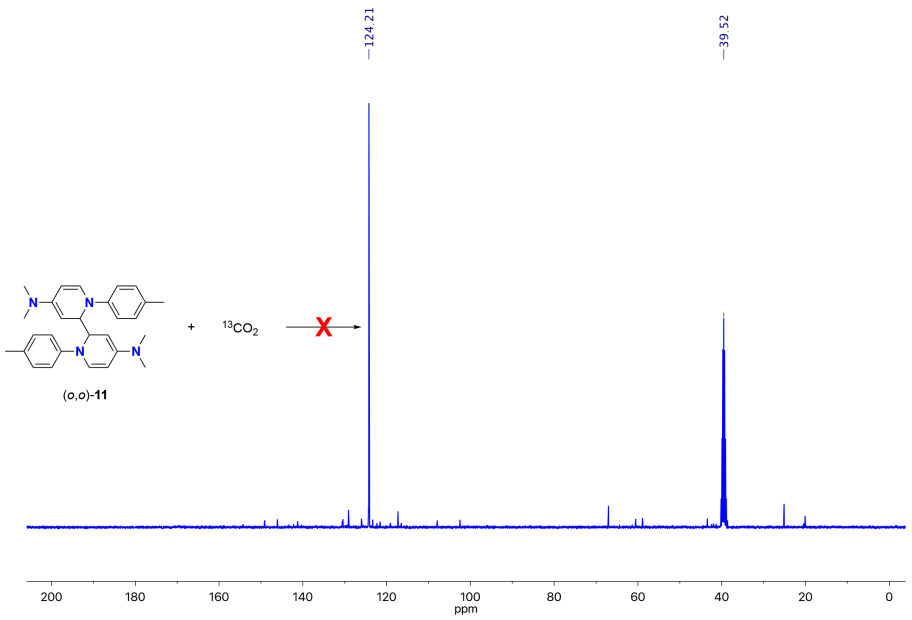

Supplementary Fig. 10 | ^{13}C NMR spectrum of the species after the reaction between $^{13}CO_2$ and tetrahydro-bipyridine dimerized from 11. Peak at 125.86 ppm corresponds to dissolved $^{13}CO_2$ in the reaction mixture.

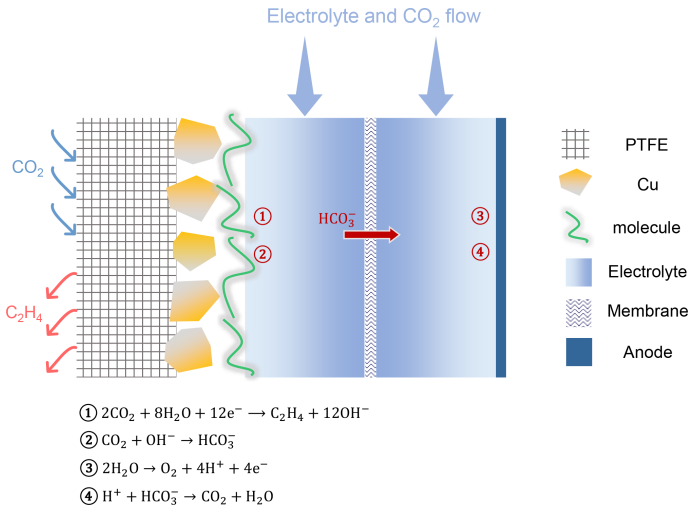

Supplementary Fig. 11 | Schematic illustration of the liquid-electrolyte flow cell and chemical reactions during CO_2RR. The flow cell consists of gas chamber, catholyte chamber, and anolyte chamber. The PTFE electrode (300 nm thick Cu with molecule functionalization) was sandwiched between CO_2 gas chamber and catholyte chamber and was used as cathode. A Ag/AgCl electrode (3 M KCl) was inserted in the cathode chamber and worked as reference electrode. A piece of Ni foam was employed as anode. Catholyte and anolyte chambers were separated by an anion-exchange membrane. Aqueous $KHCO_3$ electrolytes (1 M, saturated with CO_2) were used as both catholyte and anolyte and were circulated through the flow cell using peristaltic pumps. CO_2 was kept flowing into both catholyte and anolyte to maintain ion strength and pH during the entire electrolysis. The CO_2 gas was flowed into the gas chamber with a constant flow rate controlled by a digital gas flow controller. The gaseous products were sampled by a gas-tight syringe and analyzed by gas chromatography. A photo of the flow cell can be found in the previous report[28].

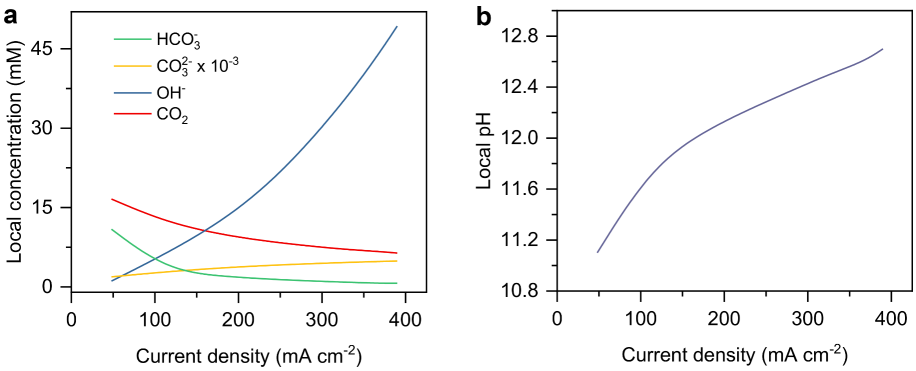

Supplementary Fig. 12 | Local species modelling in the catalyst layer at different current densities. A, Concentrations of OH^-, CO_3^{2-}, HCO_3^- and CO_2. **B**, Local pH.

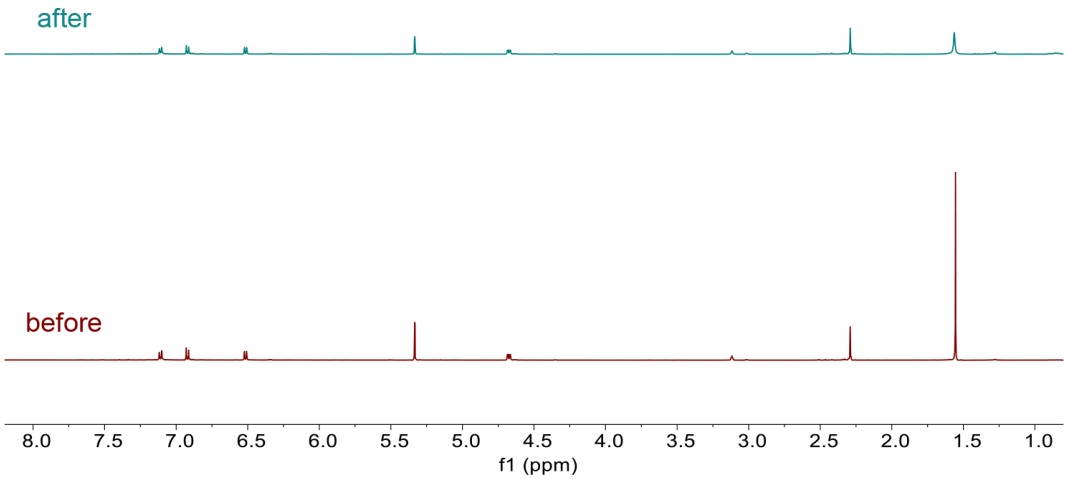

Supplementary Fig. 13 | ^{1}H NMR spectra of tetrahydro-bipyridine dimerized from 1 before and after electrolysis in 1 M KOH. The electrolysis was carried out in the liquid-electrolyte flow cell using 1 M aqueous KOH solution as electrolyte for 2 hours. The local pH is higher than that in 1 M $KHCO_3$ solution[19]. The ^{1}H NMR spectrum of the film after electrolysis was the same as the spectrum before electrolysis, suggesting that the film is resistant to OH^-. The spectrum was recorded in CD_2Cl_2 (298 K).

Supplementary Note 3 | *in situ* Raman spectroscopic measurements. Raman spectroscopy is able to identify species on a substrate with ultra-high sensitivity due to surface-enhanced Raman scattering (SERS)[29,30]. The SERS spectra were recorded at a range of applied potentials from the open circuit potential (OCP) to -0.75 V (Supplementary Fig. 14). Three regions of interest were identified as relevant to surface adsorbed CO (*CO), the coupling of which has been considered a critical step in CO_2RR to $C_{\geq 2}$ products[31-33]. The bands at 280 and 365 cm^{-1} are associated with the frustrated rotational mode of CO and the Cu–CO stretch, respectively[34]. The asymmetric region at the range of 1900–2120 cm^{-1} is attributed to the C≡O stretch of *CO[34,35]. This band is sensitive to the coordination of the *CO on the metal surface[35-37], which, in turn, may affect the activity and selectivity of the CO_2RR.

The *in situ* Raman spectra at the same applied potential, -0.72 V, on tetrahydro-bipyridine-modified Cu and pure Cu electrodes (Supplementary Fig. 15) was analyzed to assess the potential correlation among CO_2RR selectivity, CO adsorption and the electron donating properties of the *N*-aryl-substituted tetrahydro-bipyridines. The C≡O stretch band was deconvolved into two bands: *atop* bound CO (CO_{atop}, >2000 cm^{-1}, peak at ~2071 cm^{-1}) and *bridge* bound CO (CO_{bridge}, 1900–2000 cm^{-1}, peak at ~1990 cm^{-1})[35]. In *atop*, CO binds one Cu atom; in *bridge*, it binds two. The integrated areas of each band, which are proportional to the corresponding *CO coverage[36] was calculated to compare the relative population of these two kinds of Cu-bound CO.

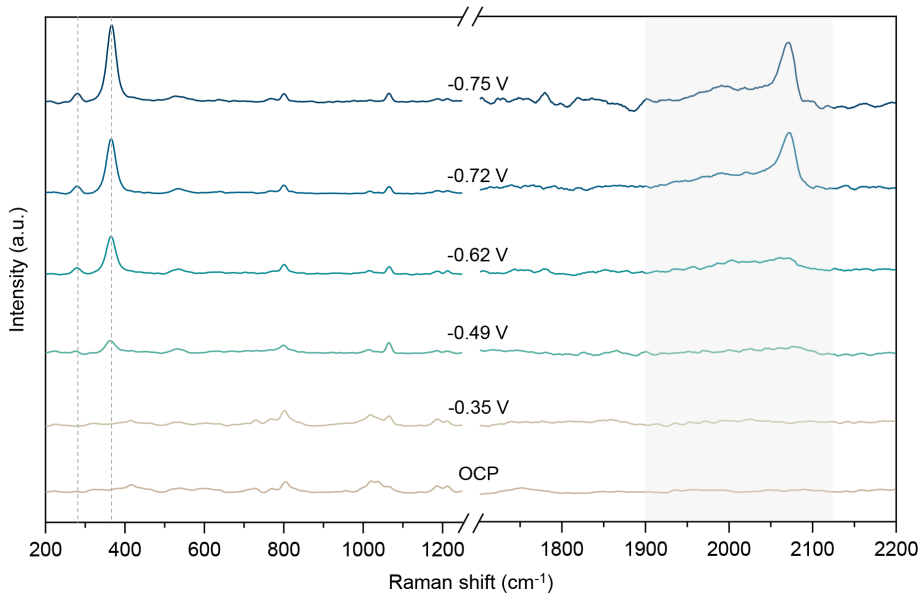

Supplementary Fig. 14 | *in situ* Raman spectra of Cu-1 under a range of applied potentials. The lines and shaded area indicate the frustrated rotational mode of CO (280 cm^{-1}), Cu–CO stretch (365 cm^{-1}) and C≡O stretch (1900–2120 cm^{-1}), respectively.

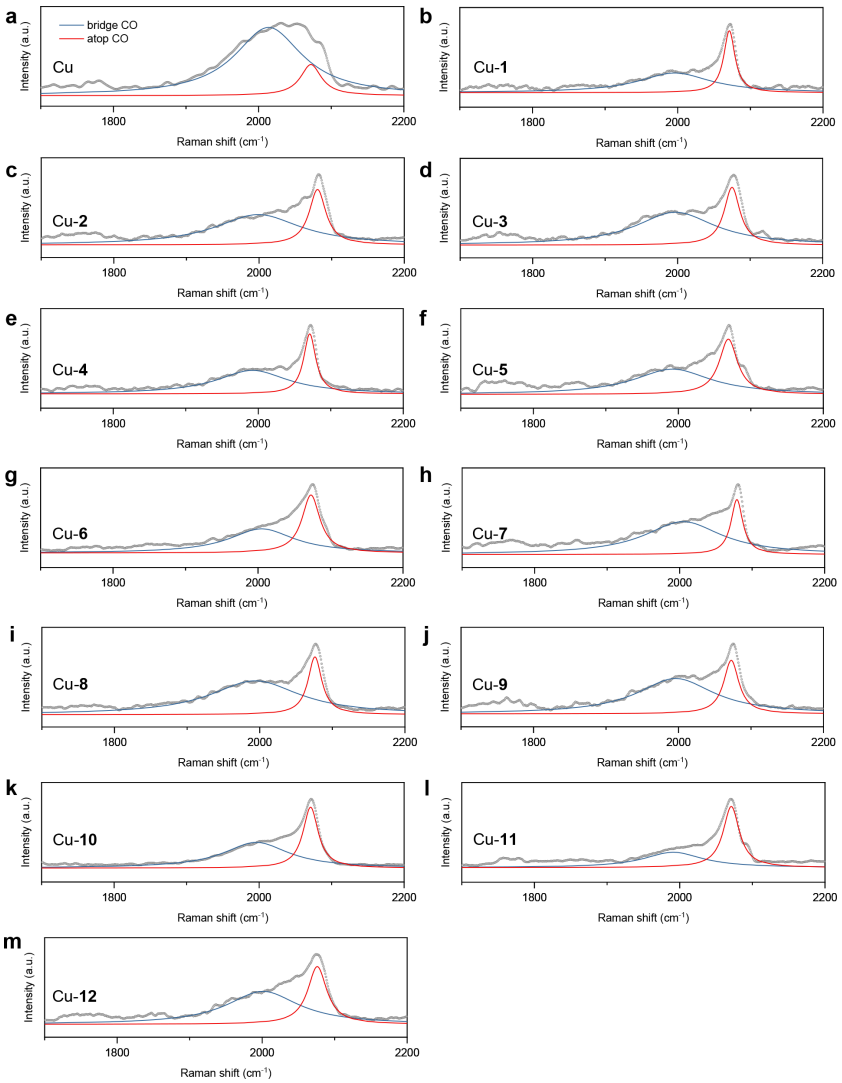

Supplementary Fig. 15 | *in situ* Raman spectra of the C≡O stretch region of Cu-x electrodes. The asymmetric band is deconvoluted into bands for *atop* CO and *bridge* CO by Lorentzian fitting. The ratio between the intensities of the two bands was summarized in Supplementary Table 2.

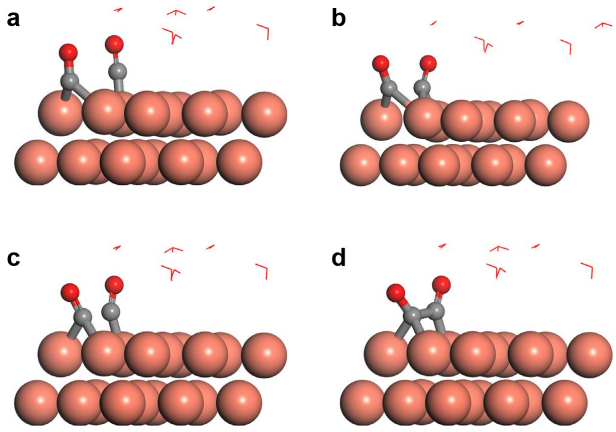

Supplementary Fig. 16 | Optimized geometries of CO and OCCO on Cu(111). a, Initial state of CO. Transient state of two CO both at *bridge* sites (**b**) and two CO at *bridge* and *atop* sites (**c**). **d**, Final state of dimerized CO, i.e., OCCO. A water layer on Cu(111) was used to capture the reaction environment. Red: O, grey: C, white: H, and pink: Cu.

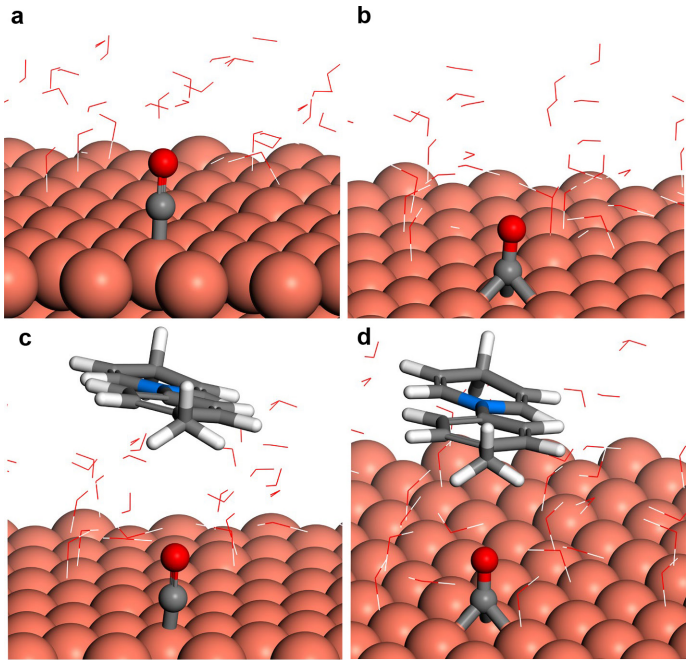

Supplementary Fig. 17 | Predicted CO adsorption geometries. Cu(111) *atop* site (**a**, **c**) and *hollow* site (**b**, **d**) without (top) and with (bottom) *N*-aryl-substituted tetrahydro-bipyridine formed from **1**. To simplify the calculations, half part of the tetrahydro-bipyridine was used. A water layer on Cu(111) was used to capture the reaction environment since a proton source near the catalyst surface is necessary for CO_2RR[38]. The *bridge* CO configuration is in equilibrium with 3-fold *hollow* site with the latter being slightly more stable than the former in the model we used[39]. Therefore, the *hollow* site is essentially equivalent to the *bridge* site observed in *in situ* Raman spectroscopy. On bare Cu(111), the *hollow* site appears to be the most stable adsorption site for CO with a CO adsorption energy (E_{CO}) of -0.39 eV, while E_{CO} on the *atop* site is only -0.13 eV (Supplementary Table 3).

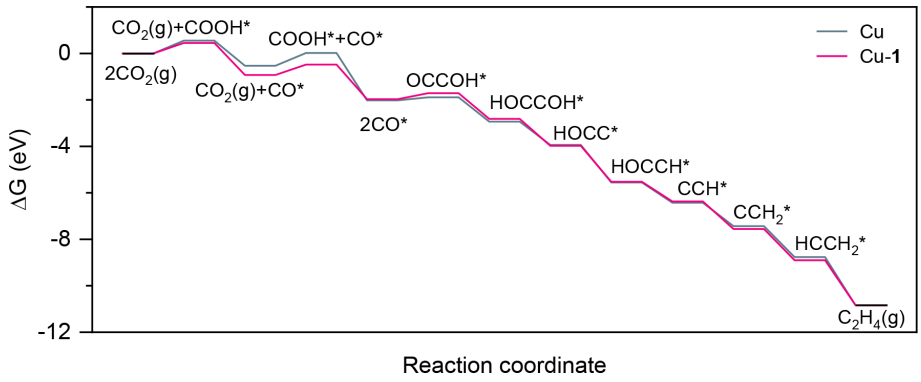

Supplementary Fig. 18 | Predicted CO_2-to-ethylene reaction pathway. Energy profile of calculated CO_2-to-ethylene pathway on Cu(111) and Cu(111)-**1** at an applied potential of -0.80 V vs. computational hydrogen electrode (CHE)[40]. The most prominent influence of the molecule on the energy profile is the enhancement of CO adsorption (lowering ΔG). This enhancement is in agreement with experimental results, in which the increased FE for ethylene comes at the expense of CO evolution on tetrahydro-bipyridine-functionalized Cu electrodes. The molecule has little influence on other steps/intermediates except that the CO_2 activation to *COOH becomes slightly more favorable after the molecular functionalization on Cu.

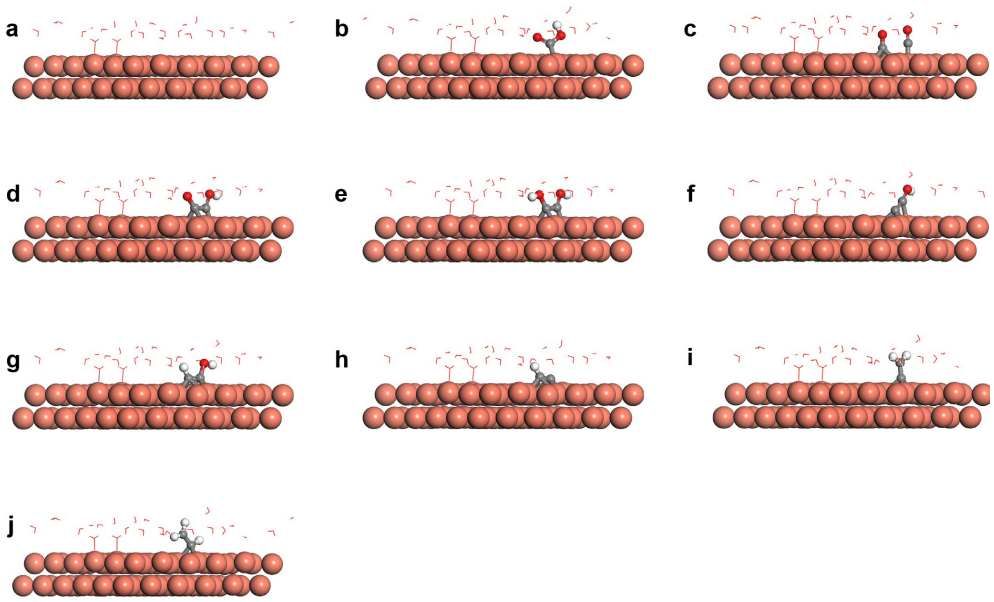

Supplementary Fig. 19 | Predicted intermediate adsorption geometries on Cu(111). A water layer on Cu(111) was used to capture the reaction environment. Red: O, grey: C, white: H, and pink: Cu.

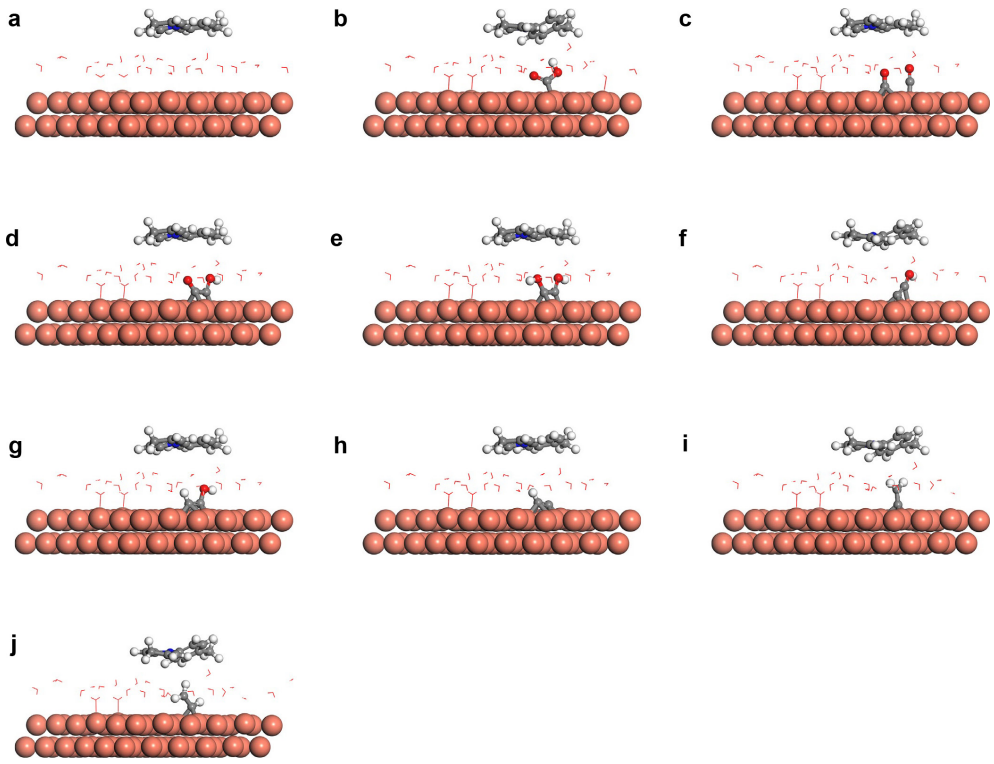

Supplementary Fig. 20 | Predicted intermediate adsorption geometries on Cu(111)-1. To simplify the calculations, half part of the tetrahydro-bipyridine was used to capture the main properties of the molecule due to its symmetric structure. A water layer on Cu(111) was used to capture the reaction environment. Red: O, grey: C, blue: N, white: H, and pink: Cu.

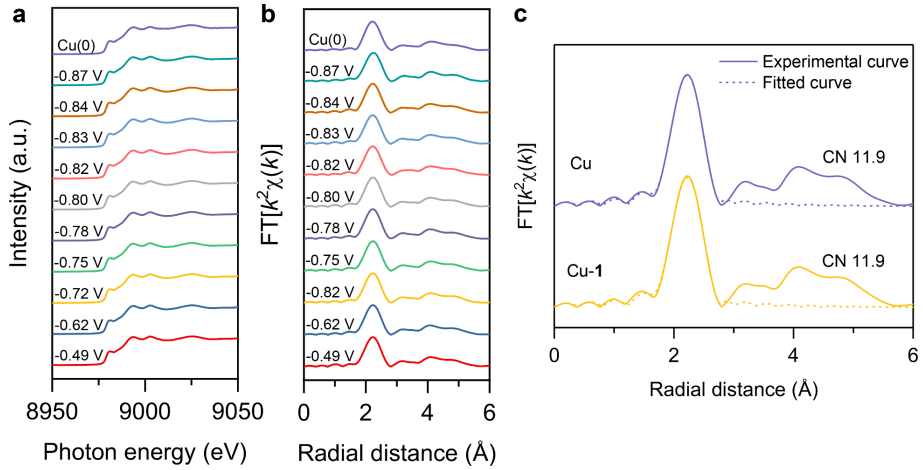

Supplementary Fig. 21 | *Operando* X-ray absorption spectroscopic analysis. X-ray absorption spectra (**a**) and Cu K-edge X-ray absorption near edge structure spectra (**b**) of Cu-**1** at applied potential range of -0.49 – -0.87 V. **c**, Coordination number (CN) fitting of Cu of pure Cu electrode and Cu-**1** electrode. *Operando* Cu K-edge spectra of Cu-**1** at both near-edge and extended-edge regions showed the existence of only Cu^0 at the applied potential range. The coordination number of Cu in the Cu-**1** sample is determined to be 11.9, the same as that of pure Cu. *Ex situ* Cu K-edge X-ray absorption spectroscopy of metallic Cu foil was performed as standard. FT: Fourier transform.

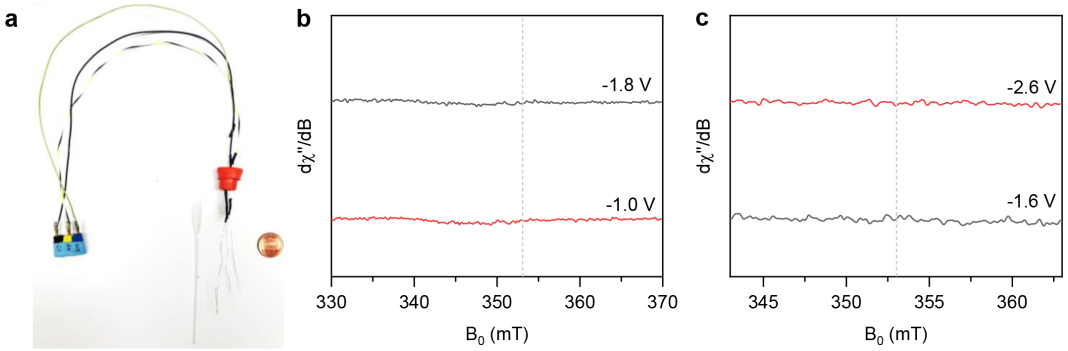

Supplementary Fig. 22 | *in situ* EPR measurements. a, A picture of the *in situ* EPR electrochemical cell. All the electrodes were inserted into a glass capillary tube (end sealed) containing electrolyte and connected to external electrochemical workstation through electric wires. A silver wire was used as a pseudo reference electrode. The potential was converted to the NHE scale using the $[Fe(CN)_6]^{3-}/[Fe(CN)_6]^{4-}$ and ferrocene/ferrocenium redox couples in corresponding aqueous and organic electrolytes, respectively. **b**, *in situ* X-band (9.879 GHz) room temperature EPR spectra at an applied potential of -1.0 V and -1.8 V *vs.* NHE in 0.1 M $KHCO_3$ solution saturated with CO_2. A Cu wire with the tetrahydro-bipyridine electrodeposited from **1** was used as the working electrode and a Pt wire was used as the counter electrode. Signals were started to sample after applying each potential for 3 minutes. **c**, *in situ* X-band (9.875 GHz) room temperature EPR spectra at an applied potential of -1.6 V and -2.6 V vs. NHE in a mixture of CH_2Cl_2 and dimethylformamide (4:6 by volume) containing 0.1 M tetrabutylammonium chloride as supporting electrolyte. The tetrahydro-bipyridine film electrodeposited from **1** was dissolved in this electrolyte by rinsing the as-deposited film on Cu foil with CH_2Cl_2. The electrolyte was saturated with N_2. Pt wires were used as the working and counter electrodes, respectively. Signals were started to sample after applying each potential for 3 minutes. The dotted line points to the magnetic field corresponding to g = 2.0, which is the typical region for organic radicals[41]. We did not observe the build-up of radicals under operating conditions, either in heterogeneous or homogeneous forms.

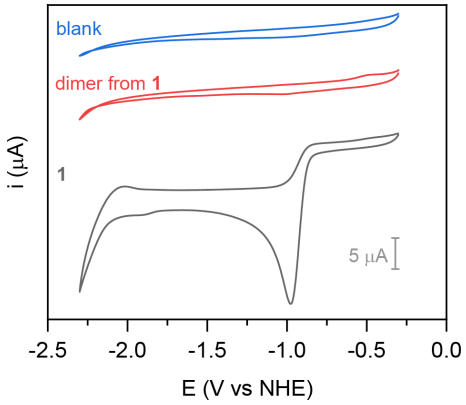

Supplementary Fig. 23 | Electrochemistry of 1 and *N*-aryl-substituted tetrahydro-bipyridine formed from 1 in organic media. Cyclic voltammetry of **1** (1 mM), tetrahydro-bipyridine dimerized from **1** (1 mM) and blank electrode in acetonitrile containing 0.1 M tetrabutylammonium hexafluorophosphate as supporting electrolyte. The electrolyte was saturated with N_2. Glassy carbon, Ag/AgCl and Pt were used as working, reference and counter electrodes, respectively. Scan rate: 100 mV s^{-1}. No reductive process was identified from the dimer species, indicating that no organic radicals from a reduction of tetrahydro-bipyridine was involved in the CO_2RR.

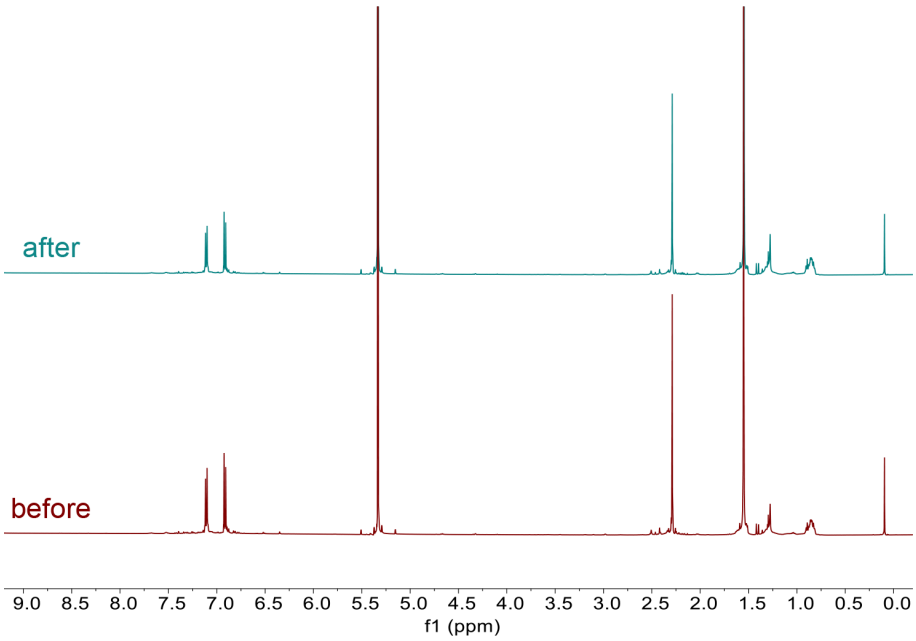

Supplementary Fig. 24 | ^{1}H NMR spectra of the tetrahydro-bipyridine dimerized from deuterated *d*5-1 before and after electrolysis. Deuterated **1**, *d*5-**1**, was synthesized from the reaction of ditolyl-iodonium triflate salt and *d*-5 pyridine as described in the Molecule synthesis part in Methods. *d*5-**1** was then electrodeposited on the PTFE/Cu electrode using the same protocol as the deposition of **1**. Electrolysis was carried out in the liquid-electrolyte flow cell under the same conditions as those for other tetrahydro-bipyridines for 1 hour. The ^{1}H NMR spectra of the film before and after electrolysis are the same, indicating that the deuterium atoms did not exchange with protons during CO_2RR. This suggests that the layer does not act as hydrogen transfer catalyst. The spectra were recorded in CD_2Cl_2 (298 K).

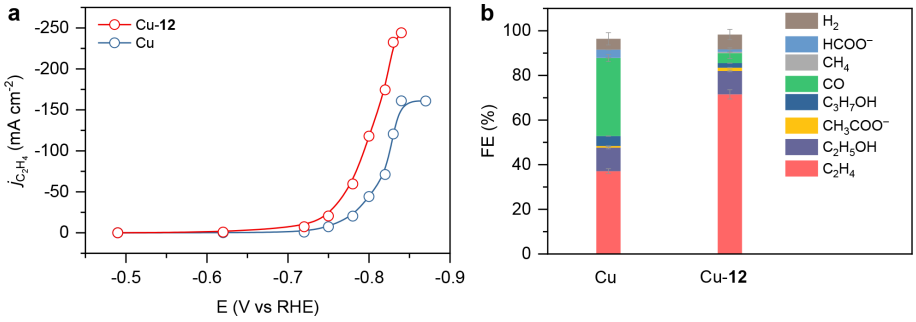

Supplementary Fig. 25 | CO_2RR performance in liquid-electrolyte flow cells. a, Partial current density of ethylene on Cu and Cu-**12** using CO_2-saturated 1 molar $KHCO_3$ as the supporting electrolyte. **b**, Product distributions on Cu and Cu-**12** at an applied potential of -0.83 V. The error bars for FE uncertainty represent one standard deviation based on three independent samples.

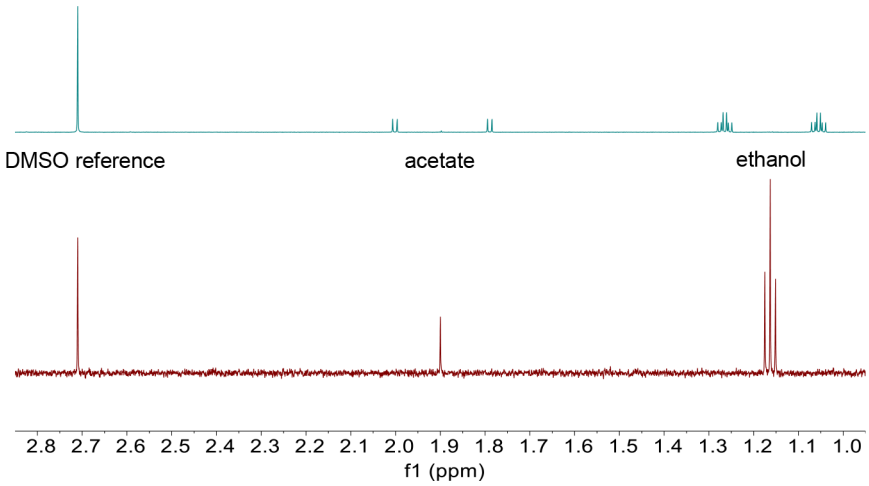

Supplementary Fig. 26 | Liquid products from isotopic CO_2 sources. ^{1}H NMR spectra of liquid products from CO_2RR using $^{12}CO_2$ (red) and $^{13}CO_2$ (cyan) as gas sources, respectively.

Supplementary Note 4 | CO_2RR in MEA. The MEA device and associated chemical reactions are illustrated in Supplementary Figs. 27 and 28. A PTFE electrode with *N*-aryl-dihydropyridine-based oligomer modified Cu (Cu-**12**) and IrO_x/Ti mesh electrode were used as cathode and anode, respectively. A Sustainion® membrane was used as anion exchange membrane (AEM). The geometric area of flow field in cathode was 5 cm^2, of which 45% is gas channel while the rest 55% is land area (Supplementary Figs. 27 and 28). 0.1 M aqueous $KHCO_3$ was flowed through anode side as anolyte and recycled during the electrolysis course. Neutral media are advantageous in terms of CO_2 utilization compared to alkaline media: if alkaline electrolyte is recycled during CO_2RR, it becomes bicarbonate eventually, due to its reaction with excess CO_2; if a single pass scheme is adopted, CO_2 is continuously consumed by alkali. In both cases, the consumed CO_2 is not easily recoverable.

Electrolysis in MEA at a range of full-cell voltages was carried out using Cu and Cu-**12** as cathodes, respectively (Supplementary Fig. 29). Similar to results in liquid-electrolyte flow cell, the functionalization of the oligomer improves the selectivity toward ethylene and this improvement comes from the decrease of FE toward CO.

The long-term stability measurement was carried at a full-cell voltage of 3.65 V. During the course of 190 hours, the current remained at ~600 mA and the average FE for ethylene was ~64%. The FEs of hydrogen and CO remain low. The pH of anolyte dropped from its initial value of 8.45 to around 7 after 20 hours, and remained at close to 7 over the whole electrolysis course (Supplementary Fig. 30).

Several reactions take place during CO_2RR. At the cathode, CO_2 is reduced to ethylene via

$$2CO_2 + 8H_2O + 12e^- \longrightarrow C_2H_4 + 12OH^-$$

The locally generated OH^- reacts with excess CO_2 via

$$CO_2 + OH^- \rightarrow HCO_3^-$$

$$CO_2 + 2OH^- \rightarrow CO_3^{2-} + H_2O$$

The generated anions transport through the AEM to anolyte. At the anode, OER takes place via

$$2H_2O \rightarrow O_2 + 4H^+ + 4e^-$$

The locally generated H^+ will react with HCO_3^- and CO_3^{2-} to form CO_2 via

$$H^+ + HCO_3^- \rightarrow CO_2 + H_2O$$

$$2H^+ + CO_3^{2-} \rightarrow CO_2 + H_2O$$

On the basis of principles of mass conservation and charge balance, the consumed CO_2 at cathode by OH^- is shuttled to the anode via HCO_3^- and/or CO_3^{2-} and released as CO_2 again, along with oxygen evolution, and the concentration of anolyte remains the same. The ratio of CO_2 to O_2 evolved from anolyte was quantified to be 69:31 by GC.

Since a large portion of CO_2 at anode was detected, the transport ions should not be OH^- only. If the transport ions are bicarbonate, the ratio of CO_2 to O_2 at the anode side should be close to 4:1, on the basis of principles of mass conservation and charge balance; if the transport ions are carbonate, the ratio should be close to 2:1. According to GC result, the experimental CO_2:O_2 ratio is closer to 2:1. Therefore, the major species transporting through the membrane is carbonate while the minor species is bicarbonate. Further, the pH at the cathode/membrane interface should be about 12 based on the pKa of carbonate.

The dissolved CO_2 concentration is calculated to be 22 mM based on Henry law

$$c = \frac{p}{p_0} \times c_0$$

where p_0 is 1 atm, c_0 is the solubility of CO_2 in 0.1 M $KHCO_3$ at 1 atm, room temperature (32 mM[42]) and p is partial pressure of CO_2 at anode side (0.69 atm based on GC result).

Then, based on the equilibrium of CO_2/ HCO_3^-/CO_3^{2-} (Supplementary Fig. 31), we could read the pH of the species of CO_2:HCO_3^- with a ratio of 22:100. The pH is 7.00. This value is very close the experimental result, indicating that our derived chemical relations are able to describe reactions during CO_2RR in MEA.

We observed a decrease of ethylene FE and, at the same time, an increase of hydrogen FE after 190 hours (Supplementary Fig. 32). To identify the possible reasons that account for this selectivity change, we characterized the cathode using XRD, XPS, SEM and energy-dispersive X-ray spectroscopic (EDS) elemental mapping (Supplementary Fig. 33). The XRD patterns of the post-electrolysis cathode are similar to those of the cathode before electrolysis, indicating that there was not significant crystalline reconstruction on a macro scale. XPS spectrum showed no iridium signal, suggesting that the increase of hydrogen FE was not caused by the deposition of iridium possibly leaching from the anode side. In the SEM image, we did see some fuzzy areas. The coupled EDS elemental analysis and mapping results indicate that these areas are potassium salts, which are likely to be K_2CO_3 based on above chemical equations and analysis. The formation of such salts is likely to be the reason for the selectivity degradation, which may block the diffusion pathway of CO_2 to the catalytic sites, decrease the local availability of CO_2, and thus increase competing hydrogen evolution reaction. We note that this is only one of the possible reasons. We also noticed liquid product crossover (Supplementary Fig. 34). The influence of this crossover issue on the properties of the membrane, such as ion transport and mechanical robustness, and hence the selectivity of CO_2RR products and stability of the device, warrants further study for practical applications.

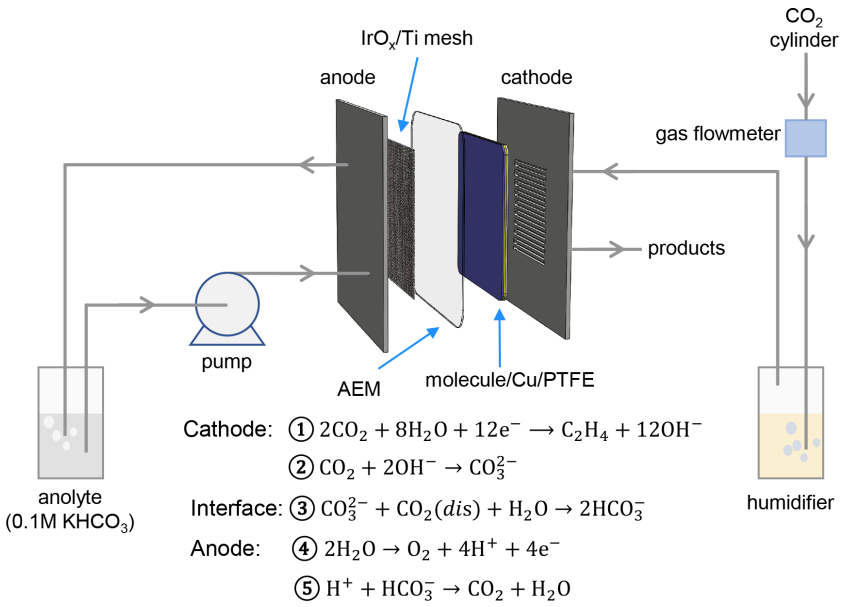

Supplementary Fig. 27 | Setup and chemical reactions for electrolysis in the MEA system. The geometric area of the cathode is 5 cm^2, of which 45% is the gas channel while the rest 55% is the land area.

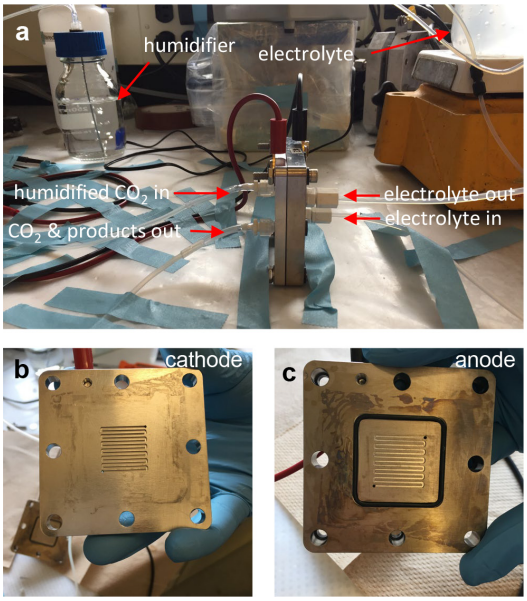

Supplementary Fig. 28 | Pictures of the MEA. a, Setup of the MEA system. **b**, Cathode flow field. **c**, Anode flow field.

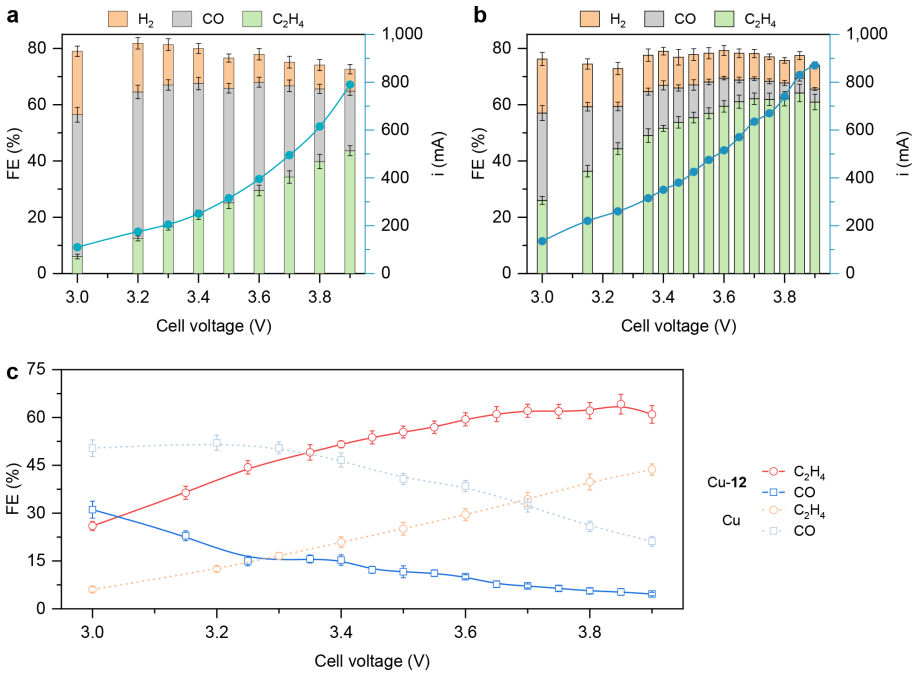

Supplementary Fig. 29 | CO_2RR in the MEA system. Gas product distribution at a range of full-cell voltage using Cu (**a**) and Cu-**12** (**b**) as cathode. **c**, Faradaic efficiency for CO and C_2H_4 on Cu and Cu-12 electrodes. The FE of CH_4 is below 1% at all voltages and was not plotted. The error bars for FE uncertainty represent one standard deviation based on three independent samples.

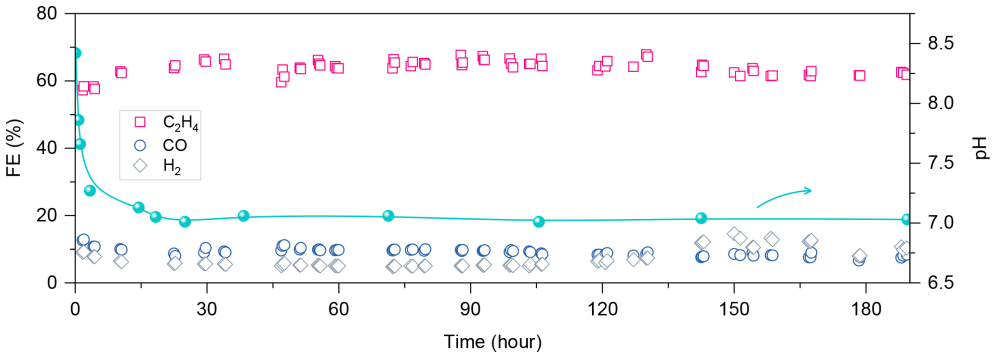

Supplementary Fig. 30 | Gas product distribution and pH of anolyte during extended electrolysis in the MEA system. The FE of CH_4 is below 1% and was not plotted.

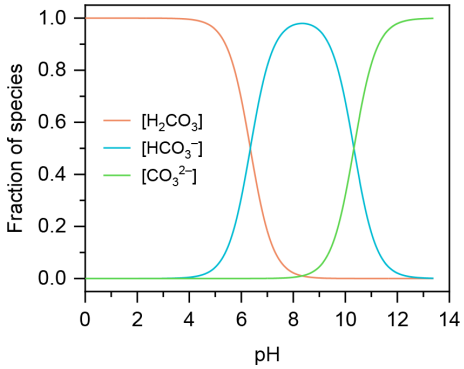

Supplementary Fig. 31 | Speciation diagram for carbonic acid system as a function of pH at 25 °C. H_2CO_3 includes both carbonic acid and dissolved CO_2 molecules, of which the latter are the major species[43].

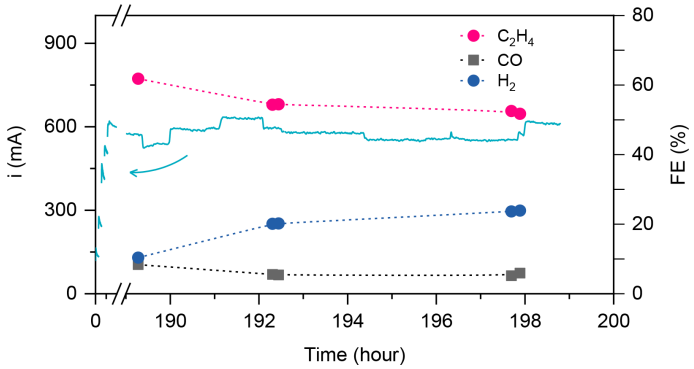

Supplementary Fig. 32 | Current and FEs of gas products after 190-hour electrolysis in MEA.

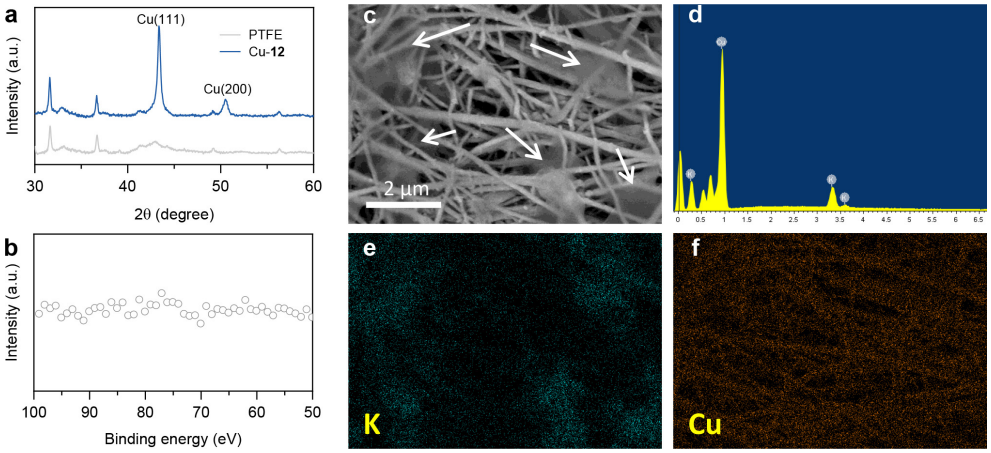

Supplementary Fig. 33 | Characterization of cathode after electrolysis in MEA. XRD patterns (**a**), XPS at the region of Ir (**b**), SEM image (**c**) and corresponding EDS elemental analysis (**d**) and elemental mapping of K (**e**) and Cu (**f**).

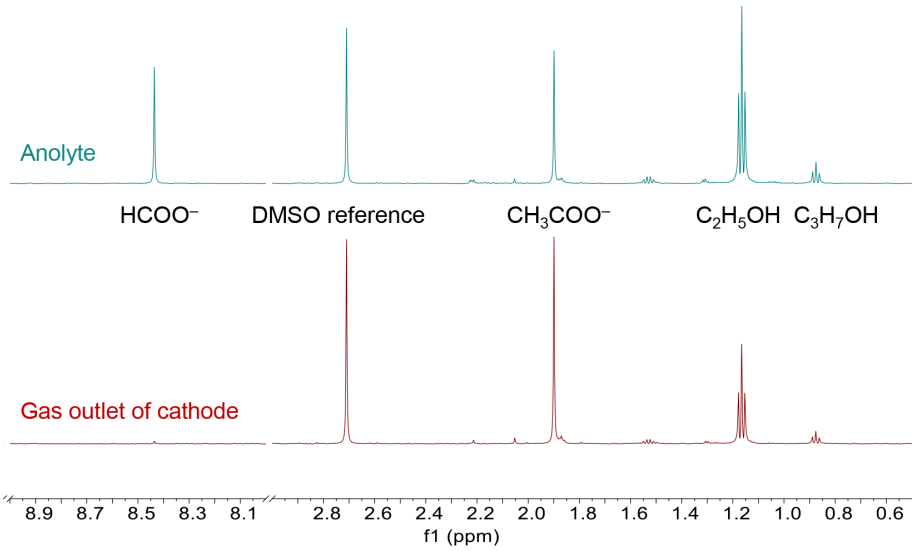

Supplementary Fig. 34 | Liquid products crossover. ^{1}H NMR spectra of liquid products collected from the anolyte and the gas outlet of cathode. The presence of all the liquid products in the anolyte indicates the crossover of these liquids, especially $HCOO^{-}$.

Supplementary Table 1 | A summary of faradaic efficiency for all products on Cu-**1** to Cu-**11** at the optimum applied potential using 1 M aqueous $KHCO_3$ (saturated with CO_2) as electrolyte. The data represent one standard deviation based on three independent samples.

Electrode	Potential (V vs RHE)	Faradaic efficiency (%)							
		H_2	$HCOO^-$	CO	CH_4	C_2H_4	C_2H_5OH	CH_3COO^-	C_3H_7OH
Cu-**1**	-0.83	7.9±2.5	2.2±0.1	5.3±2.3	0.3±0.0	64.6±1.4	16.7±0.3	3.5±0.1	2.1±0.1
Cu-**2**	-0.83	10.1±2.1	2.1±0.1	8.8±1.2	0.5±0.1	57.3±2.7	16.2±0.1	1.9±0.1	1.8±0.1
Cu-**3**	-0.83	5.1±1.3	3.3±0.1	6.3±2.0	1.8±0.0	63.1±2.4	17.6±0.4	1.1±0.0	4.7±0.1
Cu-**4**	-0.84	10.5±1.0	1.4±0.1	6.3±2.1	0.5±0.1	59.9±2.6	15.6±0.4	1.1±0.1	2.5±0.1
Cu-**5**	-0.82	22.2±1.2	3.5±0.1	4.8±3.0	0.4±0.0	50.4±2.5	15.6±0.4	2.8±0.1	2.7±0.1
Cu-**6**	-0.83	24.8±2.3	1.6±0.1	3.4±2.3	2.2±0.0	43.9±3.1	18.7±0.4	4.2±0.2	1.1±0.1
Cu-**7**	-0.83	7.5±1.5	1.9±0.1	10.1±1.3	0.8±0.0	57.0±2.8	16.2±0.4	2.1±0.1	2.5±0.0
Cu-**8**	-0.84	12.6±2.9	1.6±0.2	12.5±2.2	0.7±0.1	55.1±1.4	11.7±0.7	2.0±0.1	2.3±0.1
Cu-**9**	-0.83	13.4±2.3	1.5±0.2	12.6±2.4	0.2±0.0	55.2±2.2	12.5±0.5	1.4±0.1	2.8±0.1
Cu-**10**	-0.83	22.0±1.6	1.4±0.1	4.6±2.2	1.1±0.1	51.8±1.1	13.6±0.1	1.3±0.1	2.4±0.3
Cu-**11**	-0.82	36.7±2.7	3.7±0.2	3.5±2.5	0.3±0.0	37.5±1.3	13.9±0.1	0.9±0.1	4.4±0.1

Supplementary Table 2 | The ratio between the intensities of bands for *atop* CO and *bridge* CO. Two independent sets of samples were measured, and the average values were used for figure plotting and data analysis.

Electrode	**Ratio (atop/bridge)**		
	Tray 1	**Tray 2**	**Average**
Cu	0.141	0.130	0.136
Cu-**1**	0.487	0.470	0.479
Cu-**2**	0.359	0.343	0.351
Cu-**3**	0.352	0.364	0.358
Cu-**4**	0.435	0.409	0.422
Cu-**5**	0.521	0.543	0.532
Cu-**6**	0.661	0.673	0.667
Cu-**7**	0.257	0.251	0.254
Cu-**8**	0.264	0.272	0.268
Cu-**9**	0.301	0.289	0.295
Cu-**10**	0.553	0.539	0.546
Cu-**11**	0.729	0.748	0.739
Cu-**12**	0.465	0.471	0.468

Supplementary Table 3 | CO adsorption energy by DFT calculations.

CO adsorption site	CO adsorption energy (eV)	
	Cu(111)	Cu(111)-**1**
atop	-0.13	-0.69
hollow (bridge)	-0.39	-0.61

Supplementary Table 4 | A summary of faradaic efficiency for all products on Cu and Cu-**12** using 1 M aqueous $KHCO_3$ as supporting electrolyte. The data represent one standard deviation based on three independent samples.

Electrode	Potential (V vs RHE)	Faradaic efficiency (%)							
		H_2	$HCOO^-$	CO	CH_4	C_2H_4	C_2H_5OH	CH_3COO^-	C_3H_7OH
Cu	-0.49	45.5±1.8	n.m.	27.1±1.5	0.2±0.0	0.0±0.0	n.m.	n.m.	n.m.
	-0.62	30.9±1.4	n.m.	41.3±1.1	0.1±0.0	0.6±0.1	n.m.	n.m.	n.m.
	-0.72	18.4±1.3	n.m.	52.7±1.4	0.1±0.0	2.3±2.2	n.m.	n.m.	n.m.
	-0.75	15.3±1.6	9.0±0.3	60.3±2.5	0.0±0.0	13.2±2.6	1.9±0.1	0.3±0.0	1.0±0.0
	-0.78	10.9±2.2	7.1±0.2	55.6±1.6	0.1±0.0	16.9±1.5	2.6±0.1	0.2±0.0	2.7±0.0
	-0.80	9.4±1.5	4.4±0.4	51.9±1.7	0.1±0.0	23.5±1.3	5.9±0.1	0.4±0.0	3.4±0.2
	-0.82	6.6±2.3	4.7±0.4	46.5±2.6	0.1±0.0	27.9±2.6	6.9±0.1	0.4±0.0	3.5±0.1
	-0.83	4.9±2.8	3.7±0.1	35.0±1.6	0.1±0.0	37.1±1.1	10.5±0.5	0.8±0.0	4.5±0.1
	-0.84	5.5±1.5	3.1±0.1	24.7±1.2	0.1±0.0	43.9±1.6	15.5±0.3	1.2±0.0	3.9±0.0
	-0.87	12.7±2.0	3.0±0.2	24.7±2.1	0.1±0.0	41.2±1.6	10.4±0.2	1.1±0.0	3.8±0.1
Cu-**12**	-0.49	69.1±3.0	n.m.	14.6±1.7	0.1±0.0	0.6±0.0	n.m.	n.m.	n.m.
	-0.62	51.3±5.5	n.m.	35.2±1.3	0.1±0.0	4.2±0.8	n.m.	n.m.	n.m.
	-0.72	18.8±2.6	n.m.	43.8±1.2	0.1±0.0	20.0±1.7	n.m.	n.m.	n.m.
	-0.75	14±2.7	7.8±0.4	30.8±2.9	0.2±0.0	36.7±2.1	6.5±0.3	0.3±0	3.4±0.1
	-0.78	11.3±1.0	6.2±0.1	20.2±2.3	0.3±0.0	49.6±2.8	8.6±0.2	0.9±0	3.8±0.2
	-0.80	9.7±1.8	4.1±0.1	12.2±1.7	0.5±0.0	62.7±2.3	9.1±0.1	1.0±0.1	2.6±0.2
	-0.82	8.0±2.3	3.7±0.1	6.7±2.4	0.4±0.0	68.4±2.6	9.6±0.1	1.3±0.0	3.9±0.1
	-0.83	6.6±2.3	1.2±0.1	4.5±2.4	0.5±0.0	71.5±2.1	10.5±0.4	1.5±0.1	2.1±0.0
	-0.84	11.1±2.6	1.2±0.1	3.7±1.2	0.6±0.0	66.5±1.7	12.1±0.4	1.7±0.0	2.2±0.2

n.m. not measured.

Supplementary Table 5 | Comparision of CO_2RR to C_2H_4 performance with state-of-the-art catalysts in neural media.

Catalyst	Electrolyte	FE_{C2H4} (%)	E (V vs RHE)	j_{C2H4} (mA cm^{-2})	Ref.
Cu-**12**	**1 M $KHCO_3$**	**72**	**-0.83**	**232**	This work
Cu	1 M $KHCO_3$	44	-0.84	160	
Plasma-activated Cu	0.1 M $KHCO_3$	60[a]	-0.9	7.2	44
Boron-doped Cu	0.1 M KCl	52	-1.1	36	45
Cu-**1**, H-cell	0.1 M $KHCO_3$	41	-1.1	0.4	1
Anodized Cu	0.1 M $KHCO_3$	38	-1.08	7.3	46
Mesoporous Cu	0.1 M $KHCO_3$	38	-1.3	7.2	47
Electro-redeposited Cu	0.1 M $KHCO_3$	36	-1.2	161	48

[a]'Faradaic selectivity' (amount of specific product / amount of total detected products) instead of FE was reported, which overestimates the FE for ethylene.

Reference

1 Han, Z., Kortlever, R., Chen, H. Y., Peters, J. C. & Agapie, T. CO_2 reduction selective for $C_{\geqslant 2}$ products on polycrystalline copper with N-substituted pyridinium additives. *ACS Cent. Sci.* **3**, 853-859 (2017).

2 Ge, Q., Hu, Y., Li, B. & Wang, B. Synthesis of conjugated polycyclic quinoliniums by rhodium(III)-catalyzed multiple C–H activation and annulation of arylpyridiniums with alkynes. *Org. Lett.* **18**, 2483-2486 (2016).

3 Zhao, S., Xu, X., Zheng, L. & Liu, H. An efficient ultrasonic-assisted synthesis of imidazolium and pyridinium salts based on the Zincke reaction. *Ultrason. Sonochem.* **17**, 685-689 (2010).

4 Kitamura, T., Furuki, R., Nagata, K., Taniguchi, H. & Stang, P. J. Preparation of (p-phenylene)bis(aryliodonium) ditriflates and their double substitution by some nucleophiles. *J. Org. Chem.* **57**, 6810-6814 (1992).

5 Bielawski, M., Zhu, M. & Olofsson, B. Efficient and general one-pot synthesis of diaryliodonium triflates: Optimization, scope and limitations. *Adv. Synth. Catal.* **349**, 2610-2618 (2007).

6 Henkelman, G., Arnaldsson, A. & Jónsson, H. A fast and robust algorithm for Bader decomposition of charge density. *Comput. Mater. Sci.* **36**, 354-360 (2006).

7 Kresse, G. & Furthmüller, J. Efficient iterative schemes for ab initio total-energy calculations using a plane-wave basis set. *Phys. Rev. B* **54**, 11169-11186 (1996).

8 Kresse, G. & Furthmüller, J. Efficiency of ab-initio total energy calculations for metals and semiconductors using a plane-wave basis set. *Comput. Mater. Sci.* **6**, 15-50 (1996).

9 Kresse, G. & Hafner, J. Ab initio molecular-dynamics simulation of the liquid-metal–amorphous-semiconductor transition in germanium. *Phys. Rev. B* **49**, 14251-14269 (1994).

10 Kresse, G. & Hafner, J. Ab initio molecular dynamics for liquid metals. *Phys. Rev. B* **47**, 558-561 (1993).

11 Perdew, J. P., Burke, K. & Ernzerhof, M. Generalized gradient approximation made simple. *Phys. Rev. Lett.* **77**, 3865-3868 (1996).

12 Kresse, G. & Joubert, D. From ultrasoft pseudopotentials to the projector augmented-wave method. *Phys. Rev. B* **59**, 1758-1775 (1999).

13 Blöchl, P. E. Projector augmented-wave method. *Phys. Rev. B* **50**, 17953-17979 (1994).

14 Grimme, S., Antony, J., Ehrlich, S. & Krieg, H. A consistent and accurate ab initio parametrization of density functional dispersion correction (DFT-D) for the 94 elements H-Pu. *J. Chem. Phys.* **132**, 154104 (2010).

15 Lum, Y., Cheng, T., Goddard, W. A. & Ager, J. W. Electrochemical CO reduction builds solvent water into oxygenate products. *J. Am. Chem. Soc.* **140**, 9337-9340 (2018).

16 Dunwell, M., Yang, X., Yan, Y. & Xu, B. Potential routes and mitigation strategies for contamination in interfacial specific infrared spectroelectrochemical studies. *J. Phys. Chem. C* **122**, 24658-24664 (2018).

17 Luc, W., Rosen, J. & Jiao, F. An Ir-based anode for a practical CO_2 electrolyzer. *Catal. Today* **288**, 79-84 (2017).

18 Gupta, N., Gattrell, M. & MacDougall, B. Calculation for the cathode surface concentrations in the electrochemical reduction of CO_2 in $KHCO_3$ solutions. *J. Appl. Electrochem.* **36**, 161-172 (2006).

19 Dinh, C.-T. et al. CO_2 electroreduction to ethylene via hydroxide-mediated copper catalysis at an abrupt interface. *Science* **360**, 783-787 (2018).

20 Rumble, J. R. *CRC Handbook of Chemistry and Physics, 99th Edition (Internet Version 2018)*. (CRC Press/Taylor & Francis, Boca Raton, FL, 2018).

21 Ravel, B. & Newville, M. ATHENA, ARTEMIS, HEPHAESTUS: data analysis for X-ray absorption spectroscopy using IFEFFIT. *J. Synchrotron Rad.* **12**, 537-541 (2005).

22 Li, J. et al. Revealing the synergy of mono/bimetallic PdPt/TiO_2 heterostructure for enhanced photoresponse performance. *J. Phys. Chem. C* **121**, 24861-24870 (2017).

23 Lum, Y. & Ager, J. W. Stability of residual oxides in oxide-derived copper catalysts for electrochemical CO_2 reduction investigated with ^{18}O labeling. *Angew. Chem. Int. Ed.* **57**, 551-554 (2018).

24 Droog, J. M. M. & Schlenter, B. Oxygen electrosorption on copper single crystal electrodes in sodium hydroxide solution. *J. Electroanal. Chem. Interf. Electrochem.* **112**, 387-390 (1980).

25 Protopopoff, E. & Marcus, P. Potential–pH diagrams for hydroxyl and hydrogen adsorbed on a copper surface. *Electrochim. Acta* **51**, 408-417 (2005).

26 Cole, E. B. et al. Using a one-electron shuttle for the multielectron reduction of CO_2 to methanol: kinetic, mechanistic, and structural insights. *J. Am. Chem. Soc.* **132**, 11539-11551 (2010).

27 Chen, C.-H. et al. The "missing" bicarbonate in CO_2 chemisorption reactions on solid amine sorbents. *J. Am. Chem. Soc.* **140**, 8648-8651 (2018).

28 Zhuang, T.-T. et al. Copper nanocavities confine intermediates for efficient electrosynthesis of C3 alcohol fuels from carbon monoxide. *Nat. Catal.* **1**, 946-951 (2018).

29 Figueiredo, M. C., Ledezma-Yanez, I. & Koper, M. T. M. In situ spectroscopic study of CO_2 electroreduction at copper electrodes in acetonitrile. *ACS Catal.* **6**, 2382-2392 (2016).

30 Heyes, J., Dunwell, M. & Xu, B. CO_2 reduction on Cu at low overpotentials with surface-enhanced in situ spectroscopy. *J. Phys. Chem. C* **120**, 17334-17341 (2016).

31 Calle-Vallejo, F. & Koper, M. T. Theoretical considerations on the electroreduction of CO to C_2 species on Cu(100) electrodes. *Angew. Chem. Int. Ed.* **52**, 7282-7285 (2013).

32 Perez-Gallent, E., Figueiredo, M. C., Calle-Vallejo, F. & Koper, M. T. Spectroscopic observation of a hydrogenated CO dimer intermediate during CO reduction on Cu(100) electrodes. *Angew. Chem. Int. Ed.* **56**, 3621-3624 (2017).

33 Xiao, H., Goddard, W. A., Cheng, T. & Liu, Y. Cu metal embedded in oxidized matrix catalyst to promote CO_2 activation and CO dimerization for electrochemical reduction of CO_2. *Proc. Natl. Acad. Sci.* **114**, 6685-6688 (2017).

34 Akemann, W. & Otto, A. Vibrational modes of CO adsorbed on disordered copper films. *J. Raman Spectrosc.* **22**, 797-803 (1991).

35 Sheppard, N. & Nguyen, T. T. *Advances in Infrared and Raman Spectroscopy*. Vol. 5 67 (Heyden, London, 1978).

36 Gunathunge, C. M. et al. Spectroscopic observation of reversible surface reconstruction of copper electrodes under CO_2 reduction. *J. Phys. Chem. C* **121**, 12337-12344 (2017).

37 Gunathunge, C. M., Ovalle, V. J., Li, Y., Janik, M. J. & Waegele, M. M. Existence of an electrochemically inert CO population on Cu electrodes in alkaline pH. *ACS Catal.* **8**, 7507-7516 (2018).

38 Montoya, J. H., Shi, C., Chan, K. & Nørskov, J. K. Theoretical insights into a CO dimerization mechanism in CO_2 electroreduction. *J. Phys. Chem. Lett.* **6**, 2032-2037 (2015).

39 Guo, C., Wang, Z., Wang, D., Wang, H.-F. & Hu, P. First-principles determination of CO adsorption and desorption on Pt(111) in the free energy landscape. *J. Phys. Chem. C* **122**, 21478-21483 (2018).

40 Nørskov, J. K. et al. Origin of the overpotential for oxygen reduction at a fuel-cell cathode. *J. Phys. Chem. B* **108**, 17886-17892 (2004).

41 Gerson, F. & Huber, W. *Electron Spin Resonance Spectroscopy of Organic Radicals*. (John Wiley & Sons, 2003).

42 Wong, C. S., Tishchenko, P. Y. & Johnson, W. K. Solubility of carbon dioxide in aqueous HCl and $NaHCO_3$ solutions from 278 to 298 K. *J. Chem. Eng. Data* **50**, 817-821 (2005).

43 Zhong, H., Fujii, K., Nakano, Y. & Jin, F. Effect of CO_2 bubbling into aqueous solutions used for electrochemical reduction of CO_2 for energy conversion and storage. *J. Phys. Chem. C* **119**, 55-61 (2015).

44 Mistry, H. et al. Highly selective plasma-activated copper catalysts for carbon dioxide reduction to ethylene. *Nat. Commun.* **7**, 12123 (2016).

45 Zhou, Y. et al. Dopant-induced electron localization drives CO_2 reduction to C_2 hydrocarbons. *Nat. Chem.* **10**, 974-980 (2018).

46 Lee, S. Y. et al. Mixed copper states in anodized Cu electrocatalyst for stable and selective ethylene production from CO_2 reduction. *J. Am. Chem. Soc.* **140**, 8681-8689 (2018).

47 Yang, K. D. et al. Morphology-directed selective production of ethylene or ethane from CO_2 on a Cu mesopore electrode. *Angew. Chem. Int. Ed.* **56**, 796-800 (2017).

48 De Luna, P. et al. Catalyst electro-redeposition controls morphology and oxidation state for selective carbon dioxide reduction. *Nat. Catal.* **1**, 103-110 (2018).